

physics-informed generation methods in terms of OOD generalization. We further show that incorporating *intensity clustering* significantly enhances generalization in settings with limited label classes by producing more realistic synthetic data.

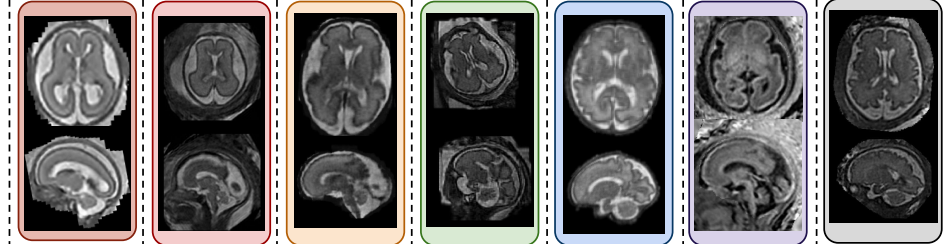
By combining synthetic pretraining with fine-tuning on real images and applying weight-space interpolation between the two models, we propose **DRIFTS** as an effective and practical solution for single-source domain generalization. **DRIFTS** consistently outperforms current state-of-the-art models across multiple benchmarks and is, to our knowledge, the first method to achieve accurate brain tissue segmentation on fetal T1-weighted images. We validate our approach on 308 subjects from four datasets acquired at three different sites, covering a range of scanner field strengths (0.55T to 3T) and both T1w and T2w modalities. We conclude with five practical recommendations to guide the development of **SynthSeg**-based methods for other organs and imaging modalities.

Keywords: Fetal Brain, Synthetic Data, Domain Randomization, Segmentation, Single-Source Domain Generalization, Fine-Tuning

1. Introduction

Fetal development is a crucial period of early life that plays an important role in shaping future physiological and neurological development (Halfon et al., 2014). Monitoring brain maturation during this period and detecting deviations from typical neurodevelopment is essential for the early detection of pathologies and timely intervention (Saleem, 2014). While ultrasonography (US) is the most widely used imaging modality for fetal examination due to its broad availability and low cost, fetal magnetic resonance imaging (MRI) is increasingly gaining prominence (Glenn and Barkovich, 2006). MRI is less operator-dependent than US and offers superior soft-tissue contrast, which is particularly valuable in studying fetal brain development, with numerous studies highlighting its potential in both healthy and pathologically developing fetuses (Jakab et al., 2021; Aviles Verdera et al., 2023; Machado-Rivas et al., 2022; Shen et al., 2022). Conditions such as ventriculomegaly, spina bifida, agenesis of the corpus callosum, cytotoxic and vasogenic edema, and intracranial hemorrhages can be effectively identified and assessed through MRI (Garel and Garel, 2004; Pfeifer et al., 2019). Although automated methods for fetal brain MRI analysis show particular promise in enabling rapid

and reliable scan processing (Uus et al., 2023), they struggle with the same limitations as most of the approaches developed for medical imaging: limited data availability and domain shifts, which are particularly pronounced in the fetal population (Dockès et al., 2021; Varoquaux and Cheplygina, 2022; Guan and Liu, 2022).



Site	KISPI (1.5T/3T)	dHCP (3T)	KISPI (1.5T/3T)	VIEN (1.5T/3T)	CHUV (1.5T)	dHCP (3T)	KCL (0.55T)
SR	IRTK	dHCP	MIAL	NiftyMIC	MIAL	dHCP	SVRTK
GA	20	21	27.3	28.4	30	28.5	38
Condition	Pathological	Healthy	Healthy	Pathological	Pathological	Healthy	Healthy
Modality	T2w	T2w	T2w	T2w	T2w	T1w	T2w

Figure 1: Illustration of the impact of various sources of domain shift in fetal super-resolution MRI across the datasets used in this study. Variations in acquisition protocols, super-resolution methods, gestational age and pathology distributions, field strengths, and specific MRI modalities contribute to distributional differences that affect model generalization.

Domain shift, or distribution shift, occurs when machine learning (ML) or deep learning (DL) models are trained on one dataset but tested on a different one with significantly varying characteristics. In MRI, domain shifts can result from variations in the imaging protocol, differences in the scanner hardware, and manufacturer disparities (Yan et al., 2020), and in fetal MRI, these parameters largely vary across centers (Kebiri et al., 2022; Xu et al., 2024; Ciceri et al., 2024). Fetal MRI poses additional challenges due to the small size of the region of interest and the high variability of brain structures, which change significantly during gestation and due to pathological processes (Stiles and Jernigan, 2010; Dubois et al., 2020), creating additional heterogeneity. Furthermore, fetal MR images are typically acquired as T2-weighted orthogonal stacks of two-dimensional (2D) slices using fast spin echo sequences, to mitigate motion artifacts. Post-processing using super-resolution (SR) reconstruction algorithms is then needed to create a high-resolution three-dimensional (3D) volume (Rousseau et al., 2010; Gholipour et al., 2010; Kuklisova-Murgasova et al., 2012; Tourbier et al., 2015; Ebner

et al., 2020). SR algorithms introduce further variability through reconstruction artifacts, use of skull stripping, and differences in image appearance and contrast, adding another layer of domain shift (Xu et al., 2023). These compounded shifts complicate training models that perform well and consistently across different datasets. Figure 1 illustrates the variability of fetal MR images related to changes in the brain morphology across maturation, acquisition parameters, magnetic field strength, and SR methodology used.

Recent results from the FeTA MICCAI challenge, presented by Payette et al. (2024a); Zalevskyi et al. (2025), demonstrate that domain shifts significantly degrade model performance when training and testing are done on different clinical datasets. The studies highlight substantial performance variability primarily driven by image quality, acquisition site, and super-resolution method, underscoring the critical need to address domain shifts in fetal MRI analysis.

Numerous techniques have been developed to address domain shifts, including diffusion-based models (Kaandorp et al., 2025; Niemeijer et al., 2024) and data augmentation strategies (Shorten and Khoshgoftaar, 2019), which aim to systematically modify or generate training images to improve model robustness to heterogeneous data. Recently, however, domain randomization (Tobin et al., 2017) techniques have seen great success in the field of MR image analysis (Billot et al., 2021, 2023b; Liu et al., 2024a). These methods begin with label maps rather than real images, generating synthetic images with randomized contrasts using Gaussian mixture models, alongside common perturbations such as geometric deformations and resampling that simulate different image resolution and partial volume effects. This strategy has demonstrated excellent OOD generalization performance, especially in MRI, a modality often challenged by substantial contrast variability across centers, scanners, and MRI sequence variants (Billot et al., 2023b).

Contributions. This work presents a comprehensive study on leveraging synthetic data for fetal brain tissue segmentation under the single-source domain generalization (SSDG) setting. We evaluate the robustness of **SynthSeg**-based models across diverse domains, scanner field strengths, and MR modalities, using data from both clinical and research settings. Building upon our previous work on **FetalSynthSeg** (Zalevskyi et al., 2024), this study extends prior findings through comparisons with physics-based simulators, additional benchmark datasets, and the integration of weight-space interpolation into a new training framework. Our key contributions are:

1. **We propose DRIFTS, a domain-robust framework for fetal brain segmentation.** DRIFTS combines synthetic training, fine-tuning on real images, and weight-space interpolation to achieve state-of-the-art performance across four independent test sets (308 subjects from three sites, spanning 0.55T–3T scanners and both T1w and T2w sequences). It consistently outperforms the FeTA 2024 challenge winner *cesne-digair*, and we systematically study its components to understand the factors driving its strong generalization.
2. **We benchmark synthetic data generation strategies for domain generalization.** We evaluate physics-based simulations using FaBiAN against GMM-based sampling and find that the latter yields better generalization. Further, we show that design choices such as *intensity clustering* and *meta-class grouping* improve segmentation robustness, and are instrumental to the performance of FetalSynthSeg.
3. **We study the benefits and limitations of fine-tuning on real images.** While fine-tuning with real data improves performance within the adapted domain, it can reduce generalization. We show that weight-space interpolation between the pre-trained and fine-tuned models mitigates this trade-off, preserving generalizable features while enhancing domain-specific accuracy.
4. **We offer practical recommendations for low-resource SSDG training.** Based on our empirical analysis, we provide actionable guidelines for building SynthSeg-based models when only single-domain labeled data is available, with recommendations that extend to other organs and imaging modalities.

The code, the trained model, and a Docker image with the model are available at <https://github.com/Medical-Image-Analysis-Laboratory/FetalSynthSeg>.

2. Background

2.1. Tackling domain shifts

Over the years, multiple approaches that follow different strategies have been proposed to tackle domain shifts. For instance, Karani et al. (2018) introduced a *transfer learning* method involving the learning of batch normalization parameters for each domain while sharing convolutional filters across

domains. This allowed models to adapt to new domains by *fine-tuning* specific parameters without altering the core network architecture. Similarly, Zhou et al. (2021) proposed a *style transfer* method that addressed domain shifts by mixing styles of source domains to implicitly synthesize novel domains, thereby diversifying training data. *Meta-learning* has also shown promise in domain generalization. Li et al. (2018) developed a model-agnostic meta-learning framework where source and target domains were simulated during training by selecting random subsamples from available source domains. This enabled the model to learn to generalize across different domains by optimizing for the learning of domain-invariant features. Additionally, Hu et al. (2023) explored *data harmonization* techniques to reduce domain shifts by standardizing data across different sources, thereby mitigating variability that could lead to performance degradation.

While these methods have been effective in various medical imaging tasks, they often necessitate a dataset of target domain images and, in some cases, annotations. In fetal MRI, obtaining such datasets can be costly and challenging (Payette et al., 2023). The manual segmentation of a single case often takes several hours of expert work (e.g., eight hours per case in Kyriakopoulou et al. (2017)). Furthermore, methods that rely on multiple source domains to learn domain-invariant features are limited when only a single training domain is available or when the diversity of available source domains does not adequately represent the target domain (Zhou et al., 2023). This limitation is especially pronounced in fetal imaging, where newly emerging scanner field strengths or SR algorithms can introduce previously unseen domains. The poor performance in these new unseen domains creates obstacles in adopting low-field ($<1\text{T}$) and ultra-low-field ($<0.1\text{T}$) MR systems, which hold great potential for democratizing access to advanced neuroimaging for broader populations (Aviles Verdera et al., 2023). The scarcity and small size of existing fetal brain imaging datasets further exacerbate this issue (Payette et al., 2023; Lajous et al., 2022).

2.2. Single-source domain generalization (SSDG)

Given these challenges, SSDG techniques are particularly relevant in the medical imaging domain. These techniques aim to train models on a *single source domain* while ensuring they can generalize well to unseen target domains. Common approaches used in medical image analysis include altering image appearance through texture and intensity augmentation and blending generated views. Ouyang et al. (2022) used randomly weighted shallow

convolutional neural networks in a global intensity non-linear augmentation (GIN) module to augment images used to learn a segmentation task. Similarly, Li et al. (2023) simulated frequency discrepancies between domains to achieve SSDG by mixing different frequency views of simulated images and incorporating a self-supervised task to learn context-aware representations.

Other approaches like the adversarial domain synthesizer (ADS) by Xu et al. (2022) synthesized new domains aimed to cover a large area of plausible distributions. They introduced a mutual information regularizer to enforce semantic consistency between synthetic domain images. Liu et al. (2022) used dictionary learning to extract prior information on the semantic shape of segmentations and images, utilizing this during test-time augmentation to improve model generalizability.

Despite advancements, SSDG still faces challenges due to the lack of diversity in training data. Current methods are limited by the semantic information in existing data and primarily focus on 2D data, with extensions to 3D image processing still unexplored. At the same time, the FeTA Challenge 2021 demonstrated that using 3D models for fetal brain tissue segmentation results in better performance than 2D models, highlighting the need for SSDG approaches applicable to 3D images (Payette et al., 2023).

2.3. Synthetic data and domain randomization

Synthetic data generation and domain randomization have emerged as promising solutions to SSDG limitations (Al Khalil et al., 2023; Paproki et al., 2024; Gopinath et al., 2024).

Synthetic data can be generated using deep learning approaches like generative adversarial networks (GANs) or diffusion models, though these methods are challenging to train and require extensive datasets to learn the latent representation of the data (Kazerouni et al., 2023; Kazeminia et al., 2020). Alternatively, numerical phantoms like FaBiAN have been developed to generate images based on physical simulations and anatomical priors such as tissue segmentation, without extensive pre-training (Lajous et al., 2022). FaBiAN, the first Fetal Brain MR Acquisition Numerical phantom, can generate multiple MR images for the same subject with varying acquisition parameters and model stochastic fetal movements, producing highly realistic images that allow for complementing scarce clinical datasets (Bhattacharya et al., 2024; Lajous et al., 2024b,a).

In contrast, **SynthSeg**, proposed by Billot et al. (2021), avoids physical simulation altogether and generates a highly diverse synthetic dataset

of images, achieving domain randomization. It uses anatomical priors but simulates tissue intensities fully randomly, creating images with unrealistic appearances. This strategy assumes that the diversity of such randomly generated data will cover the constrained diversity existing between real domains, effectively making the model agnostic to contrast. **SynthSeg** has been widely used for brain MRI analysis across various tasks, including stroke segmentation, infant and adult skull stripping, infant brain tissue segmentation, and contrast-agnostic extraction of anatomical representations of healthy and pathologically developing adult brains (Omidi et al., 2024; Kelley et al., 2024; Liu et al., 2024b,a; Shang et al., 2022; Valabregue et al., 2024; Gopinath et al., 2024).

While many synthetic data-driven approaches discussed above primarily focus on adults or infants, this work addresses fetal brain tissue segmentation, which presents unique challenges related to *in utero* imaging, including limited tissue contrast compared to postnatal imaging, often fewer annotation classes than in adult MRI, and idiosyncratic artifacts complicating the simulation of the heterogeneous fetal brain tissues.

2.4. Fetal brain tissue segmentation

The FeTA Challenge, organized as a satellite event of the MICCAI conference, plays a key role in advancing fetal brain imaging by providing a standardized platform for evaluating and benchmarking segmentation algorithms (Payette et al., 2024a; Zalevsky et al., 2025). The 2024 edition emphasized the importance of data augmentation for improving generalization across diverse multi-site datasets, as well as the use of post-processing techniques to ensure topological correctness of predicted labels. Top-performing methods employed ensembles of 3D deep learning architectures, with nnU-Net being the most commonly used. Additionally, data augmentation and synthetic data generation approaches – such as **SynthSeg** (Billot et al., 2023a) and GIN (Ouyang et al., 2022) – were adopted. The results of FeTA 2024 also highlighted the significant impact of image quality, site, and super-resolution methods on segmentation performance. The winning team, **cesne-digair**, achieved a mean Dice score of 0.816 and an HD95 of 2.317 across five testing datasets, underscoring the difficulty of the task. Their approach used a 3D U-Net implemented in the MONAI framework, trained on skull-stripped and affine-registered T2w images. Their training strategy included handcrafted spatial and intensity augmentations, along with synthetic sample generation via deformable registration between neurotypical and pathological scans.

Post-processing involved a denoising autoencoder trained to correct segmentation errors by learning from artificially corrupted manual labels, further refining the final predictions.

Using FeTA’s publicly available data, Huang et al. (2023) proposed a hybrid convolution-transformer network, achieving a Dice score of 0.837 ± 0.03 on a held-out *in-domain* validation set. Another notable approach, BOUNTI, combines 3D U-Net and Attention U-Net architectures and was trained on a large, diverse dataset of 380 fetal brain MRIs, reaching a Dice score of 0.89 ± 0.02 (Uus et al., 2023). While BOUNTI includes data from the publicly available developing Human Connectome Project, it also incorporates several additional private datasets from clinical and research studies—such as iFIND, fetal CMR, PiP, and CARP (Uus et al., 2023). Extensive manual refinement of ground truth segmentations further contributes to the model’s performance. However, the use of non-public data and a distinct annotation protocol limits the direct comparability of BOUNTI’s results with methods trained solely on the FeTA dataset.

These approaches demonstrate that robust fetal brain segmentation can be achieved through a combination of advanced data augmentation, diverse multi-site training datasets, and carefully curated annotations. While such strategies are valid and have proven effective, they often rely on extensive data resources that may not be readily available in many research or clinical settings. In contrast, our work aims to benchmark a more constrained yet common scenario: how to train models that generalize well when relying solely on publicly available, single-domain datasets with standard annotation quality. We focus on understanding the limitations of this setting and identifying effective solutions that can support generalization in the absence of large, curated training sets.

3. Materials and methods

In this section, we describe the data and approaches used for learning fetal brain tissue segmentation in our experiments.

3.1. Data

This study utilizes open-access data from the FeTA challenge (Payette et al., 2023), developing human connectome project (dHCP) (Edwards et al., 2022) as well as private clinical datasets from two institutions, summarized in Table 1. All acquisitions were performed without the use of maternal

or fetal sedation and were approved by the local ethics committee boards. In all datasets, several volumes were acquired for each subject using a 2D single-shot fast-spin-echo sequence in at least three orthogonal orientations (axial, coronal, and sagittal), to mitigate fetal motion artifacts (see *Acquisition Parameters* column in the Table 1). A super-resolution reconstruction algorithm was used afterward to merge them into a single high-resolution volume suitable for 3D volumetric segmentation.

Table 1: Dataset properties. N_n – number of neurotypical subjects, N_p – number of pathological subjects. * - Slice package duration (effective TR for slab selective IR pulse)

Site	Scanner	Acquisition Parameters	SR algorithm	Resolution (mm^3)	GA (weeks)	N_n/N_p
KISPI (public)	GE Signa Discovery MR450/MR750 (1.5T/3T)	SS-FSE	MIAL	0.5^3	20–34	25/15
		TR/TE: 2500–3500/120 ms $0.5 \times 0.5 \times 3.5 \text{ mm}^3$	IRTK	0.5^3	20–34	24/16
VIEN (private)	Philips Ingenia/Intera (1.5T) Philips Achieva (3T)*	TR/TE: 6000–22000/80–140 ms	NiftyMIC	1.0^3	19.3–34.4	33/7
CHUV (private)	Siemens MAGNETOM Aera (1.5T)	HASTE TR/TE: 1200/90 ms $1.13 \times 1.13 \times 3 \text{ mm}^3$	MIAL	1.1^3	21–35	25/15
KCL (private)	Siemens MAGNETOM FREE.MAX (0.55T)	HASTE TR/TE: 2600/106 ms $1.45 \times 1.45 \times 4.5 \text{ mm}^3$	SVRTK	0.8^3	21–35	15/5
dHCP (T2w) (public)	Philips Achieva (3T)	MB-TSE TR/TE: 2265/250 ms $1.1 \times 1.1 \times 2.2 \text{ mm}^3$	dHCP	0.8^3	21–38	248/0
dHCP (T1w) (public)	Philips Achieva (3T)	bSSFP TR/TE: 3.6/7.2 (8479*) ms $1.5 \times 1.5 \times 4 \text{ mm}^3$	dHCP	0.8^3	21–38	208/0

FeTA Challenge 2025 Datasets. Our experiments are based on several subsets of the datasets used in the FeTA 2024 Challenge. Detailed information on the acquisition protocols and dataset characteristics for KISPI, VIEN, CHUV, and KCL can be found in Table 1 and the accompanying data description papers (Zalevskyi et al., 2024; Payette et al., 2023). Each subject in these datasets was also assigned a continuous image quality score ranging from 0 (lowest) to 4 (highest), based on a standardized protocol defined in (Sanchez et al., 2024) with the results further analyzed in (Zalevskyi et al., 2025).

Fetal dHCP Dataset. Acquired at St Thomas’ Hospital, London, this dataset includes structural T2- and T1-weighted images of the fetal brain,

collected using a Philips Achieva 3T scanner equipped with a 32-channel cardiac coil (Price et al., 2019; Karolis et al., 2025). T1-weighted images were acquired using eight stacks across six unique orientations (including two repeated dynamics) with an inversion-recovery sequence and interleaved wide-slab preparation pulses. A balanced steady-state free precession (bSSFP) readout was used, with an in-plane resolution of $1.5 \times 1.5 \text{ mm}^2$, slice thickness of 4 mm, slice gap of -1.2 mm , and a flip angle of 35° , resulting in a total scan duration of approximately 8 minutes. T2-weighted images were obtained using a zoomed multiband (MB) single-shot turbo spin-echo (TSE) sequence with an MB tip-back preparation pulse. The acquisition had an in-plane resolution of $1.1 \times 1.1 \text{ mm}^2$, slice thickness of 2.2 mm, slice gap of -1.1 mm , and flip angles of either 30° or 130° , with a total duration of about 12 minutes. All T1w and T2w images were reconstructed into high-resolution isotropic 3D volumes at 0.5 mm^3 using a dedicated super-resolution (SR) algorithm from the fetal branch of the dHCP structural pipeline (Makropoulos et al., 2017).

Pre-processing and labeling. All structural images used for training and inference were resampled to an isotropic resolution of 0.5 mm^3 and standardized to a common image size of $256 \times 256 \times 256$ voxels through cropping or zero-padding. For the FeTA challenge datasets, we used the original FeTA annotations, which define seven brain tissue classes: cerebrospinal fluid (CSF), white matter (WM), gray matter (GM), subcortical gray matter (SGM), ventricles (LV), brainstem (BSM), and cerebellum (CBM) (Payette et al., 2021).

For the dHCP dataset, we manually re-mapped the original Draw-EM annotations (Makropoulos et al., 2018, 2017) to align with the FeTA label scheme using the following correspondence (Draw-EM \rightarrow FeTA): $1 \rightarrow 1$ (CSF), $2 \rightarrow 2$ (GM), $3 \rightarrow 3$ (WM), $4 \rightarrow 0$ (background), $5 \rightarrow 4$ (LV), $6 \rightarrow 5$ (CBM), $7 \rightarrow 6$ (SGM), $8 \rightarrow 7$ (BSM), and $9 \rightarrow 3$ (merged with WM). Notably, this merges the hippocampi and amygdala (label 9) with WM, and the skull (label 4) with the background. Anatomical definitions also differ slightly between the two schemes—for example, Draw-EM includes only the lateral ventricles under the "ventricles" label, while FeTA includes all four ventricles.

As a result, all final datasets include segmentation labels for seven brain tissue types, standardized according to the FeTA annotation protocol.

3.2. Methods

Our experimental framework is built upon three key components: **SynthSeg** (Billot et al., 2021), the numerical phantom FaBiAN (Lajous et al., 2022), and **FetalSynthSeg**, our customized adaptation of **SynthSeg** developed specifically for fetal brain MRI segmentation (Zalevskyi et al., 2024). Using these components, we aim to better understand how these generation strategies help mitigate domain shifts in a single-source domain generalization setting. A detailed description of each component follows.

A note on assessing generated images. Although the different models generate images from tissue segmentation, our aim is not to assess the quality of these generative approaches. Indeed, the core idea of domain randomization is to deliberately produce images with unrealistic intensities, resolutions, contrasts, and artifacts. Resulting images might appear odd to human observers, as illustrated in Figure 3. The assessment of these generative models will be done by evaluating the downstream performance of a segmentation model trained on their generated images.

3.2.1. SynthSeg

SynthSeg is a domain randomization approach that leverages anatomical segmentations rather than real images to produce synthetic data. Given a dataset of segmentations $\{S_n\}$, it randomly samples a segmentation from this dataset, which serves as an initial anatomical prior, applies spatial augmentations ϕ , and generates synthetic images G at a location (x, y, z) by sampling a Gaussian Mixture Model (GMM) defined for a label L with fully randomized parameters:

$$G(x, y, z) \sim \mathcal{N}(\mu_{L(x,y,z)}, \sigma_{L(x,y,z)}^2),$$

where μ_L and σ_L are sampled from uniform distributions $\mathcal{U}(a_\mu, b_\mu)$ and $\mathcal{U}(a_\sigma, b_\sigma)$, defined by upper and lower bounds a, b , respectively. The image is then deformed using both affine and non-rigid diffeomorphic transformations and corrupted by adding a bias field, intensity transformations and by simulating various image resolutions. By corrupting the images much more significantly than what would be realistic, **SynthSeg** ensures that the learned features will be robust to strong corruption and shifts occurring in the heterogeneous data found in practice.

3.2.2. FetalSynthSeg

Fetal brain MR images exhibit a high degree of heterogeneity and typically have a small number of segmentation classes available (e.g., seven in FeTA). Solely relying on a few annotation classes leads to images that miss finer structures, either within a class or in the background. Billot et al. (2021) noted this issue in cardiac segmentation and proposed to use intensity clustering on the background of the original (intensity) image, as well as within the different classes. This allows to simulate finer variations in the data. In **FetalSynthSeg** (Zalevskyi et al., 2024), we took this approach one step further by defining four meta-classes containing tissues with similar intensities in the original images. The meta-classes are: **white matter** (white matter, cerebellum, and brainstem), **gray matter** (cortical and deep gray matter), **cerebrospinal fluid** (ventricles and external CSF), and **non-brain tissues** (skull, uterus, fetal body, and surrounding maternal tissue) which include all non-zero image voxels that do not belong to any ground truth segmentation label. Assigning a meta-class to non-brain tissues is essential to effectively simulate the background environment surrounding the fetal brain and account for variations in SR algorithms’ performance and quality in skull stripping, ensuring that the model is trained on data that reflects realistic preprocessing variability common in fetal MRI. During the generation process, after randomly selecting the subject that will be used for generation, we first aggregate its labels into these four meta-classes. Each meta-class is then divided into a random number of subclasses, sampled from a uniform distribution $\mathcal{U}(a_{subcl}, b_{subcl})$. The splitting into subclasses is performed using the Expectation Maximization (EM) algorithm, which is conditioned on the original intensity image (Dempster et al., 1977). This process is illustrated in Figure 2. The goal of intensity-based clustering is not to generate anatomically accurate labels, but to introduce controlled, randomized intensity variability.

This strategy supports our broader objective: to *investigate how synthetic images with deliberately exaggerated or unrealistic intensity variations can enhance model generalization* beyond what is achievable with real images alone or with physics-grounded generation.

Using meta-labels and splitting them into subclasses, rather than relying on the original segmentation labels, helps prevent artificial boundaries from appearing in synthetic images that align with segmentation boundaries. This approach avoids the risk of the model learning shortcuts by relying on distinct

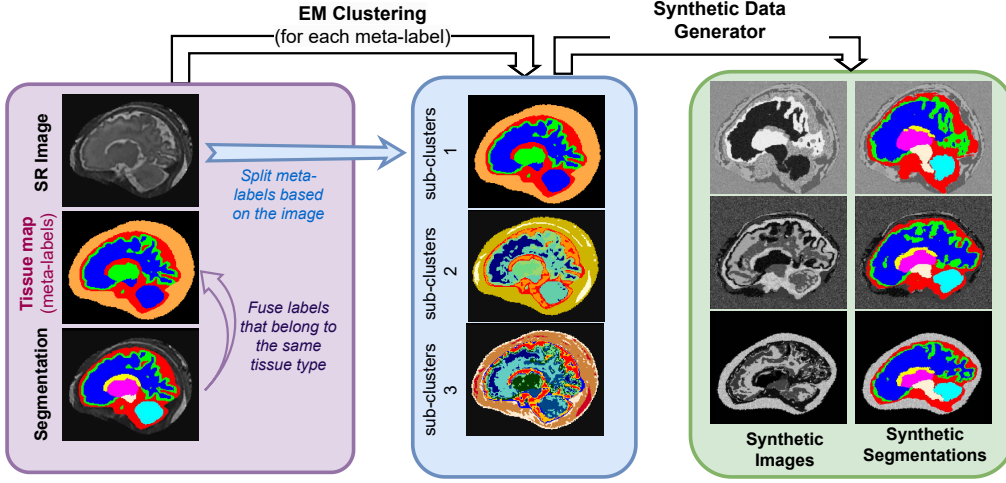


Figure 2: **FetalSynthSeg** pipeline for meta-label splitting into sub-classes. First original segmentation labels are merged into four meta-labels (WM, GM, CSF, non-brain tissue). Then, each meta-label is randomly split into sub-classes. Finally, an independent GMM is sampled for each of the sub-classes and used to sample intensities for voxels inside of it.

label contrasts that may not actually exist in real acquisitions (for example as with white matter and cerebellum that have similar intensity distributions in fetal brains (Payette et al., 2024b)).

Implementation. We implemented both the SynthSeg-based approach and our proposed FetalSynthSeg using the PyTorch version of the SynthSeg generator from the Brain-ID framework, a domain randomization method that utilizes synthetic data to learn robust brain representations (Liu et al., 2024a). All hyperparameters were retained from the original Brain-ID implementation. The generator, along with our modifications and extensions, is publicly available at: <https://github.com/Medical-Image-Analysis-Laboratory/fetalsyngen>.

3.2.3. *FaBiAN*

The Fetal Brain magnetic resonance Acquisition Numerical phantom (**FaBiAN**) is an open-source tool designed to simulate clinical T2-weighted fast spin echo (FSE) sequences of the fetal brain (Lajous et al., 2022). Like **FetalSynthSeg**, it is based on brain tissue segmentation as an anatomical prior of the fetal brain to simulate and merge the segmentation labels into coarse tissue classes (WM, GM, and CSF). However, instead of using simple

GMMs to model intensity distributions of voxels belonging to these different classes, **FaBiAN** employs the extended phase graph (EPG) formalism to simulate the signal formation process in FSE acquisitions. As such, it estimates the T2 decay over time in every voxel of the fetal brain based on the T1 and T2 relaxation times known from the literature of each of the three tissue classes, while accounting for sequence-specific mechanisms. We have modified the code of **FaBiAN** to: i) include the non-brain tissue meta-class simulated with the same subclasses as **FetalSynthSeg**, and ii) use randomized T1 and T2 values coming from a reference distribution based on the real values reported in the literature, which are then integrated into the physical simulation.

We also consider a randomized version of **FaBiAN** (**randFaBiAN**), where instead of using reference T1 and T2 values for the physical simulation, all values are sampled from a broad, unrestricted distribution. This approach randomizes the physical properties of the brain tissues, making it more akin to **FetalSynthSeg**’s method.

Figure 3 offers a visual comparison of the images generated by the discussed algorithms, while table S3 in the supplementary material details the parameters used in **FaBiAN** and **randFaBiAN**.

Implementation. We use a Matlab implementation of **FaBiAN_v2** (Lajous et al., 2024a,b) wrapped in a Python interface available on our GitHub page github.com/Medical-Image-Analysis-Laboratory/fabian_utils.

3.3. Training on real images

To assess the domain generalization capabilities of the models, we compare them to a baseline model trained exclusively on real images from the same training split. For this baseline model, we use the exact same set of real images corresponding to the segmentations used to generate synthetic images in all the other generative approaches. To ensure a fair comparison, we apply the same augmentation pipeline during training as was used for the models trained on synthetic data (including random resampling, spatial deformations and artifact generation). This setup allows us to isolate the impact of randomized intensity and contrast generation, as all other transformations—apart from intensity sampling—are applied with identical parameters across both the baseline and synthetic-data-driven models.

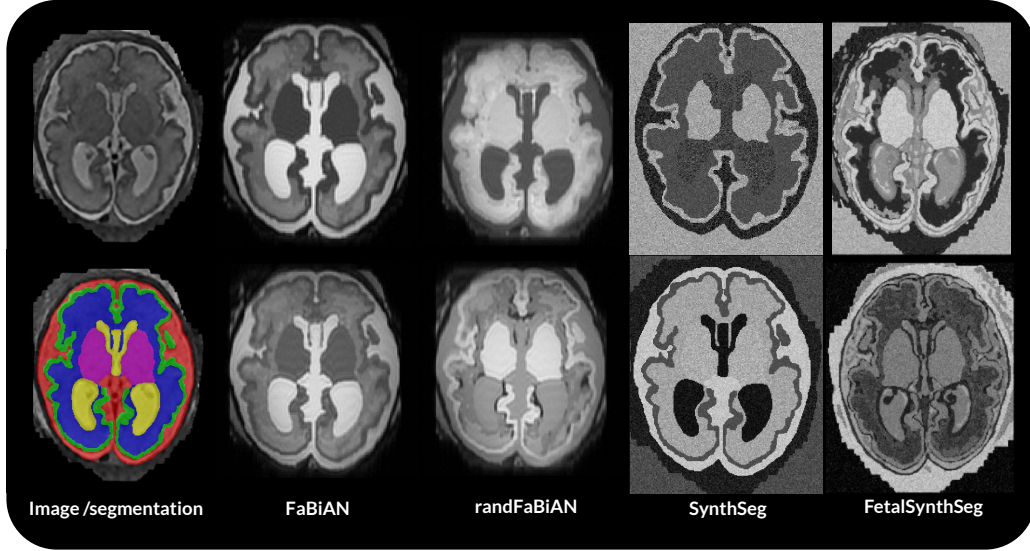


Figure 3: Examples of synthetic images generated by different data synthesis methods evaluated in this study. All methods use the same input segmentation map, and two randomly sampled outputs are shown for each to illustrate the variability introduced by the synthesis process.

3.4. Domain-Randomized Interpolated Fetal Tissue Segmentation (*DRIFTS*)

Finally, we explore how *integrating synthetic and real data* can improve the performance and robustness of segmentation models. Previous studies have shown that synthetic data is particularly valuable when real data is scarce, often achieving comparable or superior performance (Khosravi et al., 2023; Thambawita et al., 2021). Additionally, Frid-Adar et al. (2018); Loizillon et al. (2023) demonstrated that pre-training on synthetic data followed by fine-tuning with real data leverages the strengths of both data types. However, with limited real training data, fine-tuning can lead to overfitting and degrade out-of-distribution performance (Kumar et al., 2022). To address this, we explore weight-space ensembles (Rame et al., 2022; Wortsman et al., 2022a; Gagnon-Audet et al., 2023), where models pre-trained on synthetic data ($\theta_{\text{synthetic}}$) are fine-tuned with real data (θ_{real}), and their weights are linearly interpolated during inference with an interpolation rate α :

$$\theta_{\text{interpolated}} = (1 - \alpha)\theta_{\text{synthetic}} + \alpha\theta_{\text{real}}$$

This approach has been shown to enhance out-of-distribution robustness while maintaining or improving in-distribution accuracy, which is particularly

important in our experimental set-up (Wortsman et al., 2022b; Stojanovski et al., 2022). We refer to this strategy—where a model is first trained on synthetic data, then fine-tuned on real data from the same training domain, and finally combined via weight interpolation—as DRIFTS, our proposed framework for robust, domain-generalizable fetal brain segmentation.

3.5. Experimental setting

Our experiments are structured in three sections.

I — Cross-validation for selecting the synthetic data generation strategy. We first evaluate the out-of-domain generalization performance of FaBiAN, randFaBiAN, SynthSeg, FetalSynthSeg, and real-data-trained models in a cross-validation setting using fetal brain MRI. Specifically, we use two FeTA datasets: KISPI (which we subdivide into KISPI-IRTK and KISPI-MIAL based on the super-resolution algorithm applied) and CHUV-MIAL. This setup allows us to systematically assess model robustness under both site-related and super-resolution domain shift scenarios.

II — Fine-tuning to integrate limited real data with synthetic training. Fine-tuning is a widely used approach for adapting deep learning models to new domains. In this experiment, we investigate how fine-tuning, together with weight-space averaging techniques (Rame et al., 2022; Wortsman et al., 2022b; Gagnon-Audet et al., 2023), can improve the generalization performance of models trained exclusively on synthetic data. We focus on a low-resource scenario where only a small number of real images are available from a given domain.

We evaluate two fine-tuning strategies:

- **Source domain fine-tuning:** A few real images are taken from the same dataset used to generate the synthetic training data.
- **Target domain fine-tuning:** A few real images are drawn from the target (testing) domain.

In the case of target domain fine-tuning, we further examine performance across multiple target domains. Specifically, we assess how fine-tuning on one target domain affects generalization both on that domain (*in-domain*) and on other target domains that were not seen during fine-tuning (*out-of-domain*). This allows us to evaluate whether incorporating a small number of real samples from the target domain leads to domain-specific improvements or more broadly enhances model robustness.

III — Out-of-domain evaluation and comparison with state-of-the-art methods. To simulate an extreme out-of-domain generalization scenario, we compare our best-performing models to the state-of-the-art model submitted to the FeTA 2024 challenge, **cesne-digair**, which achieved the highest ranking in the competition. We evaluate both approaches on four distinct OOD datasets: the low-field 0.55T KCL dataset and CHUV dataset (both part of the official FeTA test set), as well as the dHCP T1-weighted and T2-weighted datasets. These datasets represent substantial domain shifts in terms of site and super-resolution methodology. Notably, the dHCP T1w dataset poses an especially severe domain shift, as it constitutes a different MR contrast that **cesne-digair** was not trained to handle.

To ensure a fair comparison, all models in this experiment—including ours and **cesne-digair**—are trained using the same data splits defined for FeTA 2024: the full KISPI and VIEN training sets.

Models architecture and training. In this study, we primarily aim to investigate how we can best use synthetic data generation methods for fetal brain MRI tissue segmentation. For all evaluations, we employ a 3D U-Net model, similar to the architectures in Billot et al. (2021) and Valabregue et al. (2024) implemented in Pytorch with MONAI (Paszke et al., 2019; Cardoso et al., 2022). The model includes five levels with 32 feature maps at the first level, doubling with each layer, and utilizes $3 \times 3 \times 3$ convolutions with LeakyReLU activations, except the final layer which uses softmax. Skip connections are included. We chose to focus on using a simple model and evaluating multiple data generation approaches rather than trying to build the most competitive version of synthetic data generation using larger models, ensembling or post-processing.

Training is done using the Adam optimizer with a learning rate of 10^{-3} and a loss function that combines Dice and Cross-Entropy losses, as used by Valabregue et al. (2024). Additionally, we employ the **ReduceLROnPlateau** scheduler (with a factor of 0.1 and a patience of 10 epochs) and **EarlyStopping** (with patience of 100 iterations). All experiments are conducted with a batch size of 1, implemented using the PyTorch Lightning (Paszke et al., 2019) framework, and executed using Nvidia RTX3090 and RTX6000 GPUs.

For **SynthSeg** and **FetalSynthSeg**, we generate synthetic images on the fly, training for up to 80,000 iterations. For **FaBiAN** and **randFaBiAN**, we created an offline database of 50 synthetic images per real image, resulting in 6000 synthetic images in total, and trained for a maximum of 80,000 iterations. Due to computational constraints, on-the-fly generation of **FaBiAN**

images was not feasible since the simulator, implemented in Matlab, required an average of 287 seconds to generate a single synthetic image compared to 1 second needed to generate a synthetic image with **SynthSeg** or **FetalSynthSeg**. For experiments involving real images, the training was performed for a maximum of 500 epochs to avoid overfitting.

Data augmentation. We use the data augmentations from **SynthSeg** for all of the models trained. They contain random non-linear deformation, random contrast change (Gamma transformation), random Gaussian noise, random bias field, and a random resampling simulating an acquisition at a different resolution.

Fine-tuning set-up. When performing fine-tuning, we use a pre-trained **FetalSynthSeg** model and fine-tune it on a random subset of real images (1, 3 or 5) for a maximum of 300 iterations using a small learning rate of 10^{-6} to avoid overfitting. We apply the same set of data augmentations as when training on real images. Finally, we perform weight interpolation between the fine-tuned model and the pre-trained **FetalSynthSeg** model and explore the optimal interpolation rate α that achieves the best out-of-domain generalization.

In the final out-of-domain testing experiment, we partition the full training dataset of 120 real images (from KISPI and VIEN) into a training set of 100 images and a validation set of 20 images. Fine-tuning is performed on the entire training set for a maximum of 10,000 iterations or until early stopping is triggered—defined as no improvement in validation performance for more than 5 consecutive epochs.

Cross-validation evaluation. In this experiment, we evaluate the performance of all synthetic data generation methods in a single-source domain generalization setting. We perform cross-validation using the three labeled datasets—KISPI-MIAL, KISPI-IRTK, and CHUV-MIAL—by training on one domain and testing on the remaining two. Each domain includes 40 labeled images. For each training set, we randomly assign 35 images (along with all corresponding synthetic data) for training and reserve 5 images for internal validation. All 40 images from each of the two held-out domains are used for testing. Results are reported both per target domain and as a global average across all test domains.

Metrics. We evaluate segmentation performance using two standard metrics: Dice Similarity Coefficient (Dice) and the 95th-percentile Hausdorff Distance (HD95) (Zalevskyi et al., 2025). These metrics capture different aspects of agreement between the predicted and ground truth (GT) segmen-

tations:

- **Dice Similarity Coefficient (DSC):** Measures voxel-wise overlap between the predicted and GT segmentations. It is defined as:

$$DSC = \frac{2 \cdot |A \cap B|}{|A| + |B|}$$

where A and B are the predicted and ground truth voxel sets for a given label. Higher Dice values indicate better overlap.

- **95th-percentile Hausdorff Distance (HD95):** Captures the spatial discrepancy between segmentation boundaries, defined as:

$$HD95 = \max \left(\max_{x \in A} \min_{y \in B} \|x - y\|, \max_{y \in B} \min_{x \in A} \|x - y\| \right)$$

where A and B are the boundary point sets of the predicted and GT segmentations, and $\|\cdot\|$ denotes the Euclidean distance. Lower HD95 values indicate better boundary agreement.

Statistical analysis. We use a non-parametric Wilcoxon rank-sum test with Bonferroni correction to statistically analyze the results and compare the performance of the same subjects using different methods. A p-value for statistical significance is set to 0.05.

4. Results

4.1. Cross-validation experiment

The global comparison of the methods is available in Table 2. Solely considering the performance of the methods, on average **FetalSynthSeg** outperforms all competitors by a large margin, showing how synthetic data generation can help bridge the gap between domains. We report additional per-label metric results and HD95 values for these experiments in the Supplemental Materials Tables S4 and S5. Several more insights drawn from these results are presented in the following.

Table 2: Mean Dice scores (multiplied by 100 for readability) for models trained on different data sources, evaluated across multiple testing splits. Each cell reports the mean and standard deviation across test subjects. **Bold** indicates the best-performing method per column, and underlined denotes the second-best. An asterisk (*) marks cases where the best method is statistically significantly better than the second best according to a Wilcoxon rank-sum test ($p < 0.05$).

Testing split	CHUV-mial		KISPI-irtk		KISPI-mial		Global
Training split	KISPI-irtk	KISPI-mial	CHUV-mial	KISPI-mial	CHUV-mial	KISPI-irtk	
FaBiAN	74.2±4.2	73.1±5.7	53.6±13.3	56.6±12.9	60.6±17.1	61.5±20.1	63.3±15.5
randFaBiAN	<u>79.1±2.3</u>	<u>78.2±2.9</u>	55.1±12.7	68.9±7.8	60.7±7.3	<u>68.1±14.7</u>	68.3±13.8
SynthSeg	75.9±3.9	73.7±3.9	<u>70.9±9.2</u>	<u>74.8±7.8</u>	60.5±15.7	63.4±16.8	72.2±13.0
FetalSynthSeg	80.7±2.0*	76.9±3.3	79.2±9.0*	76.8±6.9*	<u>67.5±16.0</u>	68.5±15.6	74.9±11.5*
Real Data	77.2±4.0	78.5±3.3*	70.6±13.9	71.9±11.5	68.0±19.3	64.3±19.1	<u>73.0±12.6</u>

4.1.1. Intensity clustering is key to achieving a strong performance

As the FeTA segmentations contain only seven classes, using just the initial segmentation does not allow to fully capture the intricate details of real images. Using the original image and generating additional classes through intensity clustering allows us to tackle this issue. This is what we show in Figure 4. This figure shows how performance varies for **SynthSeg** and **FetalSynthSeg** depending on the number of sub-classes used for intensity clustering. **SynthSeg** with one sub-class is the default model. There is a clear benefit of using multiple sub-classes per tissue, independently of the choice of using meta-labels. Nevertheless, we see that the meta-labels allow **FetalSynthSeg** to retain a small edge over **SynthSeg**. A statistical analysis reveals that **FetalSynthSeg** still outperforms **SynthSeg** in 7 out of 12 training splits, with **SynthSeg** performing better in 3 splits, and no significant difference in performance found in the remaining 2 splits.

4.1.2. Data quality greatly impacts generalization performance

Table 2 also shows a large variance in performance across splits, but also across subjects, with a variance up to 16 Dice points for the CHUV-mial trained **FetalSynthSeg** model tested on KISPI-mial data. Focusing on **SynthSeg** and **FetalSynthSeg**, Figure 5 shows the heterogeneity from the different testing splits. It is very clear, especially for KISPI-MIAL, that pathological subjects can be much harder to successfully segment than healthy ones (Figure 5(B)), which is mostly correlated to image data quality: all methods fail at segmenting reconstructed images that had been rated to have poor quality. This is clearly illustrated by Figure 5. However, **data quality does**

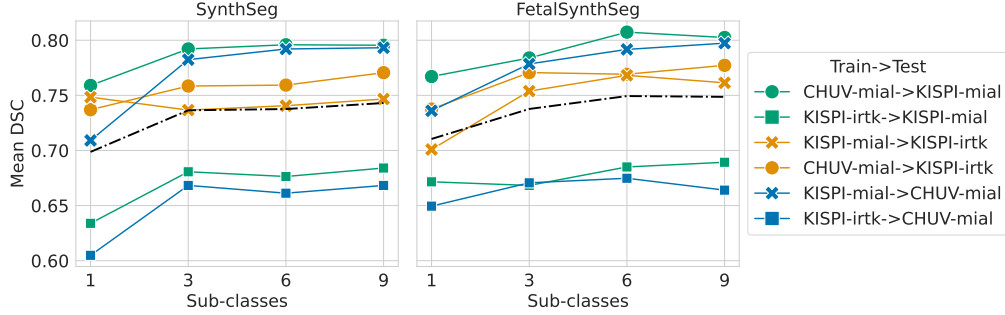


Figure 4: Ablation study on the number of subclasses used. For **SynthSeg**, the original 7 labels used as generation classes are randomly split into 1-9 subclasses, while in **FetalSynthSeg** the meta-labels are split. We report mean Dice across all tissues for each combination of training-testing splits. The dashed line gives the average trend.

not only impact the evaluation but also learning: models trained using the lower quality KISPI-MIAL data also lead to a lower generalization performance across all splits (cf. Table 2).

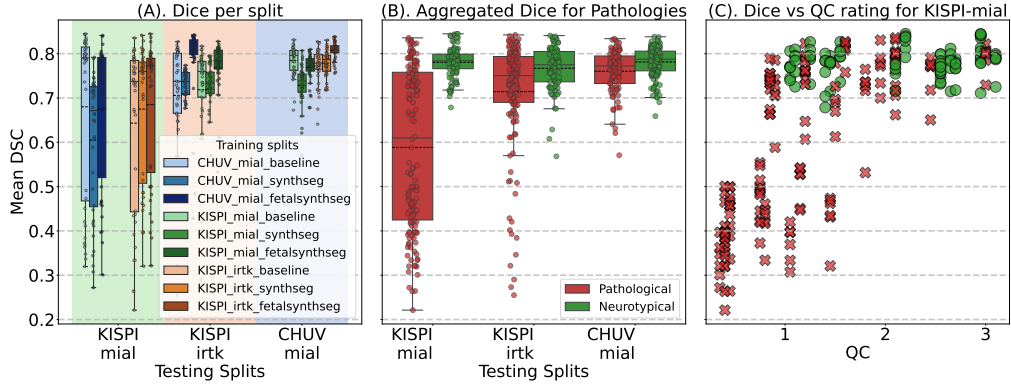


Figure 5: (A) Performance comparison between the baseline model trained on real images, **FetalSynthSeg**, and **SynthSeg**. (B) Distribution of Dice scores for each model on the testing splits, grouped by subject status (healthy vs. pathological). (C) Impact of image quality on model performance on the KISPI-mial split.

4.1.3. *SynthSeg-based approaches outperform physics-based simulation for model training*

Table 2 also features an ablation study on four different variants for synthetic generation. The results show that **FaBiAN**, which restricts intensity simulation to reference tissue relaxometry properties generalizes worst (63.3 Dice). **randFaBiAN** simulates a wider range of T1 and T2 tissue values, and largely increases its performance to (+5; 68.3 Dice). **SynthSeg** then moves from using **FaBiAN** as a simulator to GMM gains and allows to get an additional edge (+3.9; 72.2 Dice). The final gain comes from using meta-classes (+2.7; 74.9 Dice). The role of **SynthSeg**-based data augmentations is also investigated in the Supplementary Experiment S1, where we show how it improves the performance of models even when using real images and is superior to the standard augmentations based on MONAI that are commonly used in the field.

These results suggest that there is a gap between **FaBiAN**-based approaches and **FetalSynthSeg**. This is further supported by Supplementary Experiment S2, where a **FetalSynthSeg** model trained using 6000 samples like **FaBiAN** still outperforms it by 3.9 Dice points. It is also important to remember that **FaBiAN**-based contrast simulation requires very heavy and slow computations (around 280 seconds per subject), compared to the simple and extremely efficient contrast simulation using GMMs. This makes physics-based generators like **FaBiAN** impractical for the online generation used in **SynthSeg**-based approaches.

Qualitative analysis in Figure 6 illustrate these findings, showing that models with randomized contrast generators like **randFaBiAN** and **FetalSynthSeg** are more robust to domain shifts, particularly when there is a mismatch in skull-stripping quality between training and testing data.

4.2. *DRIFTS experiments*

Our next series of experiments explores the potential benefits of combining real and synthetic data for enhancing out-of-domain generalization, which is a key part of the proposed **DRIFTS** framework. First, we examine whether incorporating additional data from the source (training) domain can further improve model performance. Next, we assess the impact of augmenting the training set with a limited number of target domain samples. Throughout these experiments, we compare standard fine-tuning and weight averaging techniques to evaluate their effectiveness.

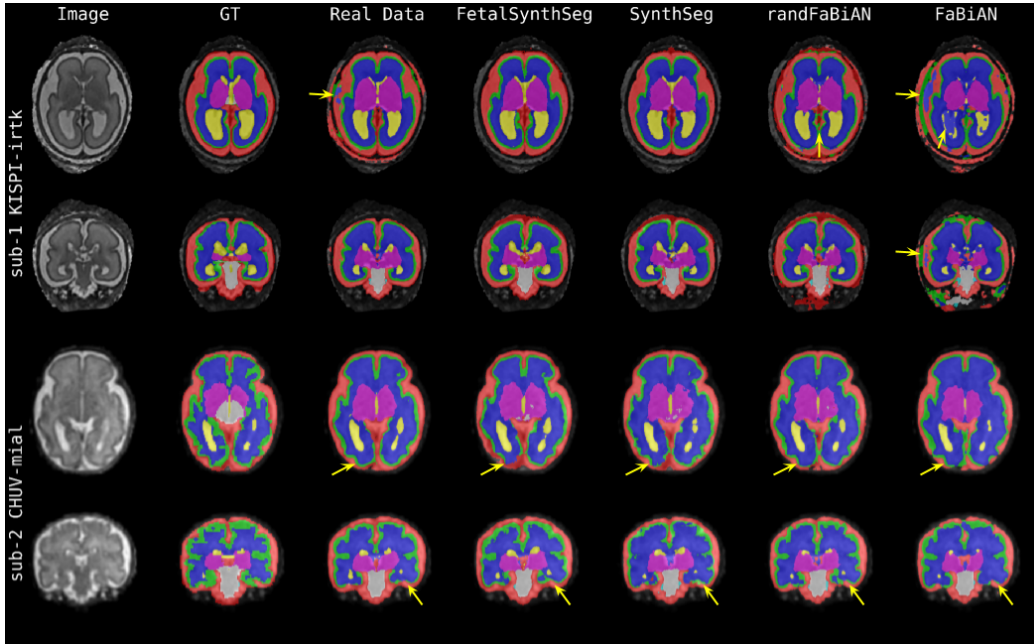


Figure 6: Segmentation results for models trained on the KISPI-MIAL data split, evaluated on a subject from the KISPI-IRTK split (top; excellent quality) and on another from the CHUV-mial split (bottom; acceptable quality). Arrows point to regions of substantial discrepancies across models.

4.2.1. Source domain fine-tuning marginally improves the generalization performance of *FetalSynthSeg*

Figure 7 shows the results obtained when fine-tuning *FetalSynthSeg* on real data from the training domain and compares it to the weight-space interpolation. The results show that fine-tuning with real images from the same domain that was used for pre-training with synthetic data often does not *significantly* improve generalization performance and that it can even lead to performance drops in some cases. These limitations are mostly overcome by averaging the weights of the original and fine-tuned models. Overall, the weight-interpolated models show a statistically significant improvement in mean Dice score over both the original and fine-tuned models across two of the three evaluation splits. However, in the case of training on KISPI-IRTK and testing on KISPI-MIAL we notice a strong decrease in the performance of fine-tuned model (-2.5 Dice), showing the risk of overfitting to a particular training split when fine-tuning the model on real images. Nevertheless, by

averaging the weights of the **FetalSynthSeg** and the fine-tuned model, we can recover from the performance dropped, and improve performance for other splits.

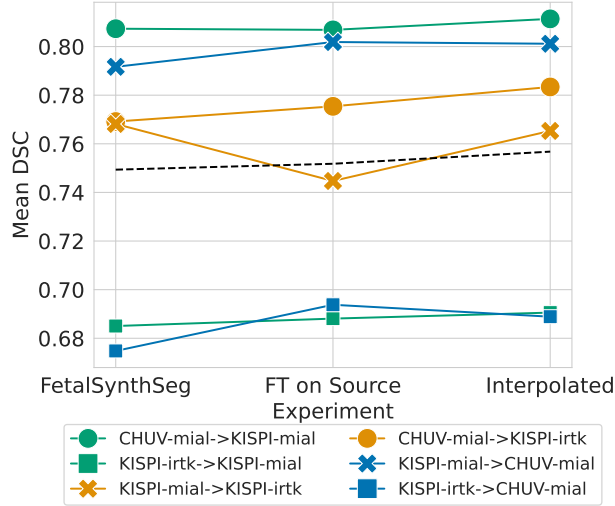


Figure 7: Mean Dice for models trained on the source domain. *FetalSynthSeg* – trained only on synthetic data from the source domain. *FT on Source* – are **FetalSynthSeg** models trained first on the synthetic data and then fine-tuned on the same source domain. *Interpolated* – weight averaging of the two first models.

4.2.2. Target domain fine-tuning and weight averaging improve generalization to other domains

Additionally, we investigated how using a few annotations from real images of a *target* domain impacts the generalization of **FetalSynthSeg**. We evaluated the fine-tuned model both on the target domain used for fine-tuning, and also on other unseen before domains. In Figure 8, we observe that weight averaging improves target domain performance compared to vanilla fine-tuning ($\alpha = 1$), but also improves generalization to *other domains*, which does not occur with vanilla fine-tuning. Averaging weights with $\alpha = 0.5$ or 0.8 yields both a large target domain improvement (up to +5 in Dice with 3 images) which then translates into an improvement up to +1 Dice in other domains. Vanilla fine-tuning only improved performance in the target domain setting, while the performance in other domains remained unchanged, or even declined due to overfitting.

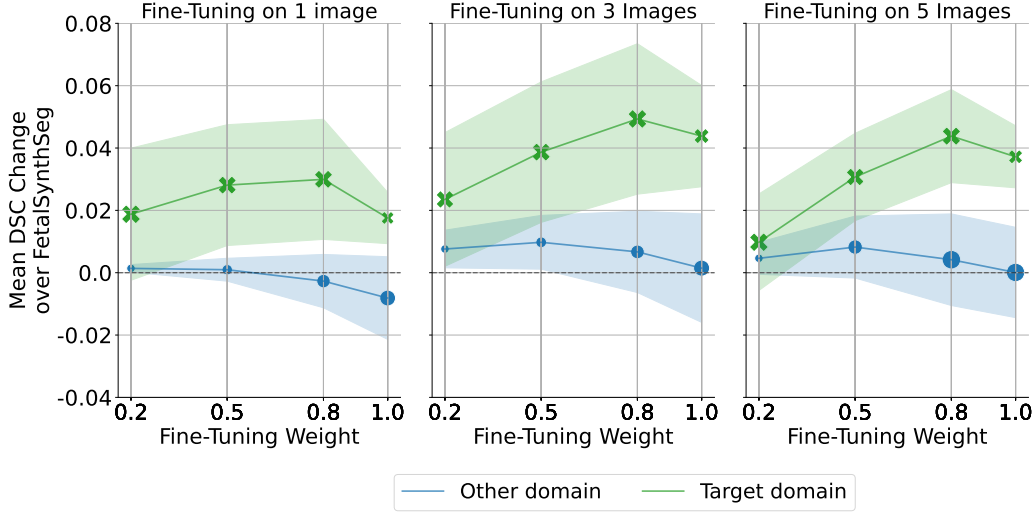


Figure 8: Improvement in Dice of the fine-tuned target domain data compared to the **SynthSeg** performance. We evaluate how fine-tuning with different numbers of images $\{1, 3, 5\}$ affects the performance of the fine-tuned model as well as its interpolated version with different interpolation weights. We evaluate the performance both in the target domain and in other domains. Fine-tuning weight α is the weight that is used for averaging: $\theta_{\text{interpolated}} = (1 - \alpha)\theta_{\text{FetalSynthSeg}} + \alpha\theta_{\text{fine-tuned}}$. The original **FetalSynthSeg** is at $\alpha = 0$ and vanilla fine-tuning is at $\alpha = 1$.

4.3. OOD testing and SoTA comparison

Finally, to assess the effectiveness of the best reviewed approach, we compared it against the state-of-the-art model that won the FeTA 2024 Challenge. Specifically, we evaluated the **DRIFTS** model, which is obtained by weight-averaging a **FetalSynthSeg** model trained on synthetic data and its fine-tuned version trained on the full FeTA real dataset with $\alpha = 0.5$ as shown to be optimal from our previous experiments.

As shown in Figure 9, fine-tuning enhances performance on in-domain data (FeTA test set and dHCP T2w), but leads to a substantial performance drop on out-of-distribution data (dHCP T1w). In contrast, the **DRIFTS** model consistently outperforms the FeTA 2024 winner across all four test datasets, with the most significant improvement observed on the dHCP T1w images—where the winning model’s performance notably deteriorates. We provide a qualitative comparison of the described models in the Figure 10 as well as the HD95 and per-label results in the Supplementary materials Table S6, Figure S1, and Table S7 respectively.

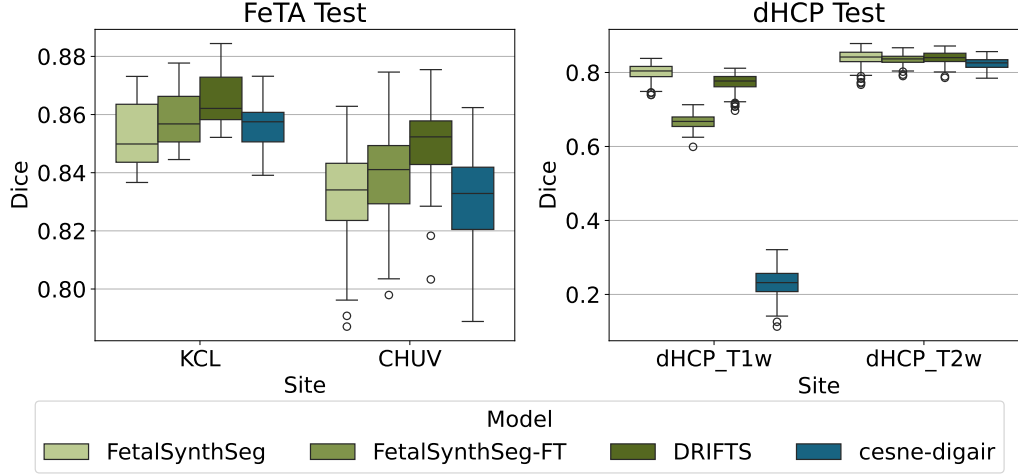


Figure 9: Performance comparison between **cesne-digair** (FeTA 2024 challenge winner), **FetalSynthSeg**, **FetalSynthSeg** fine-tuned on the full FeTA 2024 training set, and the proposed **DRIFTS** approach (weight interpolation of the two) on the FeTA 2024 test sets and the dHCP T1w and T2w scans.

Table 3 presents the DSC scores for the evaluated models across multiple institutions and imaging modalities. **DRIFTS** achieves the best overall performance on all test datasets, except for the dHCP T1w images. On this challenging out-of-domain contrast, the domain-randomized **FetalSynthSeg** model performs best, while the fine-tuned model suffers a significant drop in accuracy and **cesne-digair** fails completely.

Table 3: Dice scores (mean \pm std, 1–100 scale) on FeTA test sets (CHUV, KCL) and dHCP (T1w, T2w). The best Dice for each dataset-contrast pair is shown in **bold**, and the second best is underlined.

Dataset	MR contrast	cesne-digair	FetalSynthSeg	FetalSynthSeg-FT	DRIFTS
CHUV	T2w	83.0 \pm 1.8	83.2 \pm 1.6	<u>83.9\pm1.6</u>	84.9\pm1.4
KCL	T2w	85.6 \pm 0.9	85.2 \pm 1.2	<u>85.9\pm1.0</u>	86.5\pm0.9
dHCP	T1w	23.2 \pm 3.8	80.1\pm2.1	66.7 \pm 1.9	<u>77.4\pm2.2</u>
dHCP	T2w	82.4 \pm 1.5	84.0\pm2.0	<u>83.6\pm1.3</u>	84.0\pm1.6

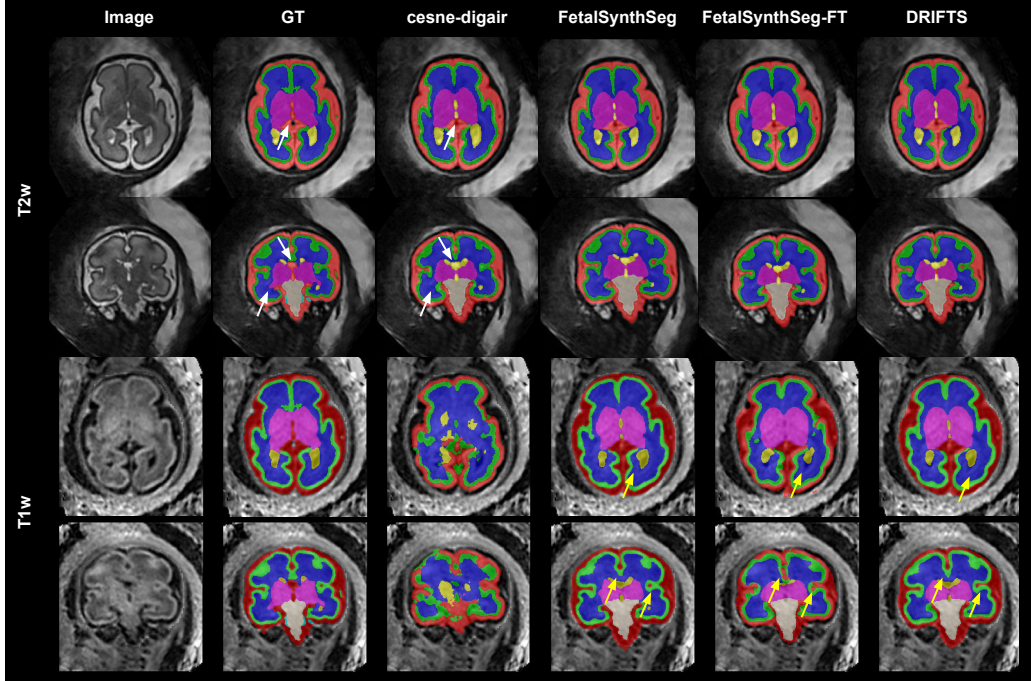


Figure 10: Qualitative comparison of the proposed models and *cesne-digair* on a test case from the dHCP dataset, showing T2w images (top two rows) and T1w images (bottom two rows) from the same subject. White arrows highlight discrepancies between the dHCP and FeTA annotation schemes—particularly in the definitions of SGM and LV—as all models were trained using FeTA annotations, while the ground truth reflects dHCP labels converted to FeTA format. Yellow arrows indicate prominent segmentation errors made by the model fine-tuned on real T2w images when applied to the T1w contrast.

5. Discussion

This paper proposed a combination of domain randomization and weight interpolation (DRIFTS) to best leverage synthetic data to train robust models capable of generalizing across fetal brain MRI domains. We conducted a careful analysis in a SSDG setting in the task of fetal brain tissue segmentation. Building on *SynthSeg* (Billot et al., 2021, 2023a), our experiments examined the impact of data generation strategies, intensity clustering, and fine-tuning on real images in the context of single-source domain generalization. The challenges encountered in fetal brain MRI—such as limited dataset size and significant domain shifts caused by varying acquisition protocols and super-resolution algorithms—are common across many areas of medical imaging.

Through a comprehensive evaluation involving over 300 subjects from three distinct datasets, spanning two MR contrasts, and covering both clinical and research populations with normal and pathological cases, we provide insights that can inform the adaptation of **SynthSeg**-based methods to new anatomical targets and imaging modalities. We revisit hereafter the main outcomes of our work.

(i) Intensity clustering is essential for a strong performance of domain randomization. In our experiments, intensity clustering led to a substantial improvement in performance—approximately a 5-point gain in Dice score—which proved essential for enabling **SynthSeg**-based methods to outperform models trained on real data. Moreover, these synthetic models demonstrated greater robustness when evaluated on out-of-domain volumes acquired at 0.55 T, reconstructed with previously unseen super-resolution algorithms, or originating from unseen imaging modalities. This has initially been used in the cardiac context in (Billot et al., 2023b), and our results as well as others in the literature (Valabregue et al., 2024) confirm its crucial importance when few label classes are available.

(ii) Meta-classes can further improve the performance of the domain randomization method. In our experiments, meta-classes allowed **FetalSynthSeg** to get a small but statistically significant edge over **SynthSeg** (~ 2 DSC point). They illustrate a good trade-off between pure domain randomization and physics-based constraints that can be imposed. If different classes contain the same type of tissues (e.g., CSF is found in both tissues around the brain and ventricles of the brain), their intensity distributions are expected to be similar within the same domain. Simulating different intensities for these tissues can lead to the waste of model capacity.

(iii) Physics-based intensity generation methods do not improve performance compared to Gaussian mixture models When considering data generation procedures, it was clear that using **FaBiAN** (Lajous et al., 2022) with realistic physical parameters did not allow to achieve strong generalization performance. However, **randFaBiAN**, with randomized parameters, reached a much better performance of 68.4 DSC on average. This was still below **SynthSeg** (72.2 DSC), which benefited from a larger randomization by sampling intensities directly from a GMM. Indeed, it is easier to obtain large tissue intensity variations by directly sampling their values from a GMM than by randomizing tissue properties like T1 and T2 values in **FaBiAN**.

(iv) Data quality greatly impacts the generalization ability of synthetic methods. Models trained on KISPI-IRTK data consistently out-

performed those trained on KISPI-MIAL data, which had worse data quality (Zalevskyi et al., 2025). This observation aligns with the better reported performance obtained with the BOUNTI method on their testing split, caused by the higher quality annotations (Uus et al., 2023), and the failure of **SynthSeg**-based approaches on poor quality data (Billot et al., 2023b; Valabregue et al., 2024).

(v) Fine-tuning the model on a few segmentations from another domain boosts the performance of the model in-domain and *also* out-of-domain. Fine-tuning experiments showed the potential of fine-tuning the model on a few pairs of (image, segmentation) for a new domain (as demonstrated in other work (Lhermitte et al., 2024)), and using weight-averaging to improve the performance both on the new domain *and* for other domains. Techniques based on weight-averaging have seen great successes in computer vision and for large language models (Wortsman et al., 2022a; Rame et al., 2022; Ramé et al., 2023; Yadav et al., 2024), and could be promising ways to fine-tune models like **SynthSeg** and **FetalSynthSeg** in a community-driven manner, by only responsibly sharing the weights of fine-tuned models across multiple centers, without having to share any data. Indeed, contrarily to common fine-tuning, our results show that weight-averaging can bypass the trade-off between in-domain and out-of-domain performance: increasing in-domain performance with weight-averaging does not have to lead to a loss in out-of-domain performance.

(vi) DRIFTS demonstrates clear added value with strong generalization to unseen domains, as evidenced by our model’s robust performance on the dHCP T1w dataset. Unlike the FeTA 2024 winner, *cesne-digair*, which suffers a significant performance drop, **FetalSynthSeg** and **DRIFTS** maintain high accurate results, even on this challenging contrast where tissue contrast is notably poor (Brugger et al., 2006).

Furthermore, weight interpolation can help mitigate catastrophic forgetting (Kirkpatrick et al., 2017). In our experiments, fine-tuning **FetalSynthSeg** on real T2w images led to a clear case of forgetting: the model’s performance on the dHCP T1w dataset deteriorated significantly. This suggests that the generalizable features acquired through domain-randomized pretraining were overwritten by contrast-specific features during fine-tuning. While fine-tuning improved performance on the T2w contrast, it came at the cost of reduced generalization to T1w scans.

Weight interpolation between the original **FetalSynthSeg** and its fine-tuned variant helped to mitigate this issue. As shown in Figure 8, tuning

the interpolation ratio allows one to balance domain specificity and generalization, thereby optimizing performance across domains. Notably, even in-domain, the interpolated DRIFTS model outperforms both of its individual components, suggesting the emergence of beneficial properties from interpolation, consistent with prior findings in Ortiz-Jimenez et al. (2023). However, the performance of the DRIFTS model on T1w images remains lower than that of the original **FetalSynthSeg**, indicating that the effectiveness of weight interpolation depends on the degree of domain shift between the fine-tuning and testing datasets. This highlights the importance of carefully selecting interpolation parameters to achieve optimal performance across diverse domains.

Limitations and future work. While thorough, our experiments are limited to fetal brain MRI segmentation. Although we believe that it is an excellent test bed with datasets of limited size and strong domain shifts, it is possible that not all of the observations will generalize to other settings. We have attempted to limit this issue with rigorous cross-validation and using a held-out pure testing sets. As done by Billot et al. (2023a), we did *not* investigate the influence of model architectures on the generalization of the model. Although we expect these observations to hold independently of the model architecture chosen, there could be unexpected, more subtle dependencies.

In our experiments, we employed simple generative methods that synthesize images by sampling intensities from GMM-based segmentation maps. While these methods are fast and computationally efficient, they depend heavily on predefined parameters and prior assumptions about domain shift sources. In contrast, more advanced techniques, such as stable or conditional diffusion models, offer a data-driven alternative by learning to generate images from learned priors. These approaches present a promising direction for future research beyond **SynthSeg**-style generation. However, their substantial computational demands make real-time, on-the-fly generation impractical (Wang et al., 2023). Given our focus on efficient single-source domain generalization, a thorough comparison with diffusion-based models falls outside the scope of this work.

Beyond understanding more clearly how to train a synthetic data model, future work will aim at building a stronger version of **FetalSynthSeg**, by leveraging a larger amount of data and multi-stage architectures like in (Billot et al., 2023b), focusing on the topological correctness of the predicted segmentations and performance in the cases of severe pathologies. This will be a first step towards developing robust segmentation tools that could be

widely used across different demographics, scanners, magnetic field strengths, and MR contrasts.

6. Conclusions

This study investigated how to effectively leverage synthetic data for robust fetal brain MRI segmentation under single-source domain generalization. We evaluated a range of strategies—including synthetic data generation methods, intensity clustering, meta-class grouping, and weight-space interpolation—which collectively enabled state-of-the-art performance across four diverse test datasets.

To our knowledge, this is the first work to achieve high-quality segmentation on T1-weighted fetal MR images using synthetic training data. Our DRIFTS model outperformed the FeTA 2024 benchmark across multiple domains, including unseen scanners, super-resolution pipelines, and modalities.

These results provide a practical foundation for building scalable, domain-robust segmentation tools applicable to a wide range of clinical and research settings.

Declaration of competing interest

The authors declare that they have no known competing financial interests or personal relationships that could have appeared to influence the work reported in this paper.

Data availability

The KISPI and dHCP are publicly available dataset (Payette and Jakab, 2021; Edwards et al., 2022). KCL and CHUV datasets used for evaluation in this study are part of the private testing set from the FeTA challenge and are not publicly accessible. VIEN data is not publicly available.

CRedit author statement

Vladyslav Zalevskyi: Conceptualization, Investigation, Methodology, Software, Visualization, Writing – Original Draft Preparation. Thomas Sanchez: Conceptualization, Software, Visualization, Writing – Review & Editing, Supervision. Margaux Roulet: Software, Methodology, Writing – Original Draft

Preparation. Hélène Lajous: Software, Methodology, Writing – Review & Editing. Jordina Aviles Verddera: Investigation, Data Curation. Jana Hutter: Investigation, Data Curation, Funding Acquisition. Roxane Licandro: Investigation, Data Curation, Funding Acquisition. Georg Langs: Investigation, Data Curation, Funding Acquisition. Gregor Kasprian: Investigation, Data Curation, Funding Acquisition. Hamza Kebiri: Writing – Review & Editing, Supervision. Meritxell Bach Cuadra: Funding Acquisition, Supervision, Writing – Review & Editing.

Acknowledgments

This research was funded by the Swiss National Science Foundation (182602 and 215641), ERA-NET Neuron MULTI-FACT project (SNSF 31NE30 203977), UKRI FLF (MR/T018119/1) and DFG Heisenberg funding (502024488); we acknowledge the Leenaards and Jeantet Foundations as well as CIBM Center for Biomedical Imaging, a Swiss research center of excellence founded and supported by CHUV, UNIL, EPFL, UNIGE and HUG. This research was also supported by grants from NVIDIA and utilized NVIDIA RTX6000 ADA GPUs.

The Developing Human Connectome Project (dHCP) was funded by the European Research Council (ERC) under the European Union’s Seventh Framework Programme (FP7/2007–2013), Grant Agreement No. 319456. The Wellcome Centre for Integrative Neuroimaging is supported by core funding from the Wellcome Trust [Grant No. 203139/Z/16/Z]. The views expressed in this work are those of the authors and do not necessarily reflect those of the NHS, the NIHR, King’s College London, or the Department of Health and Social Care. The authors gratefully acknowledge the families and participants involved in the dHCP, as well as the neonatal staff at the Evelina Newborn Imaging Centre, St Thomas’ Hospital, Guy’s & St Thomas’ NHS Foundation Trust, London, UK, for their work in acquiring and processing the data.

Declaration of generative AI and AI-assisted technologies in the writing process

During the preparation of this work, the authors used Grammarly and ChatGPT (GPT 4o) to assist with spell checking, grammar refinement, and language clarity improvements. After using this tool/service, the authors

reviewed and edited the content as needed and take full responsibility for the content of the publication.

References

- Al Khalil, Y., Amirrajab, S., Lorenz, C., Weese, J., Pluim, J., Breeuwer, M., 2023. On the usability of synthetic data for improving the robustness of deep learning-based segmentation of cardiac magnetic resonance images. *Medical Image Analysis* 84, 102688. URL: <https://www.sciencedirect.com/science/article/pii/S1361841522003164>, doi:<https://doi.org/10.1016/j.media.2022.102688>.
- Aviles Verdera, J., Story, L., Hall, M., Finck, T., Egloff, A., Seed, P.T., Malik, S.J., Rutherford, M.A., Hajnal, J.V., Tomi-Tricot, R., Hutter, J., 2023. Reliability and feasibility of low-field-strength fetal mri at 0.55 t during pregnancy. *Radiology* 309. URL: <http://dx.doi.org/10.1148/radiol.223050>, doi:10.1148/radiol.223050.
- Bhattacharya, S., Price, A.N., Uus, A., Sousa, H.S., Marenzana, M., Colford, K., Murkin, P., Lee, M., Cordero-Grande, L., Teixeira, R.P.A., et al., 2024. In vivo t2 measurements of the fetal brain using single-shot fast spin echo sequences. *Magnetic resonance in medicine* 92, 715–729.
- Billot, B., Greve, D.N., Puonti, O., Thielscher, A., Van Leemput, K., Fischl, B., Dalca, A.V., Iglesias, J.E., 2021. Synthseg: domain randomisation for segmentation of brain scans of any contrast and resolution. *arXiv preprint arXiv:2107.09559* .
- Billot, B., Greve, D.N., Puonti, O., Thielscher, A., Van Leemput, K., Fischl, B., Dalca, A.V., Iglesias, J.E., et al., 2023a. Synthseg: Segmentation of brain mri scans of any contrast and resolution without retraining. *Medical image analysis* 86, 102789.
- Billot, B., Magdamo, C., Cheng, Y., Arnold, S.E., Das, S., Iglesias, J.E., 2023b. Robust machine learning segmentation for large-scale analysis of heterogeneous clinical brain mri datasets. *Proceedings of the National Academy of Sciences* 120, e2216399120.
- Brugger, P.C., Stuhr, F., Lindner, C., Prayer, D., 2006. Methods of fetal mr: beyond t2-weighted imaging. *European Journal of Radiology* 57, 172–181.

URL: <http://dx.doi.org/10.1016/j.ejrad.2005.11.017>, doi:10.1016/j.ejrad.2005.11.017.

Cardoso, M.J., Li, W., Brown, R., Ma, N., Kerfoot, E., Wang, Y., Murrey, B., Myronenko, A., Zhao, C., Yang, D., et al., 2022. Monai: An open-source framework for deep learning in healthcare. arXiv preprint arXiv:2211.02701.

Ciceri, T., Casartelli, L., Montano, F., Conte, S., Squarcina, L., Bertoldo, A., Agarwal, N., Brambilla, P., Peruzzo, D., 2024. Fetal brain mri atlases and datasets: A review. *NeuroImage* 292, 120603. URL: <https://www.sciencedirect.com/science/article/pii/S1053811924000983>, doi:<https://doi.org/10.1016/j.neuroimage.2024.120603>.

Dempster, A.P., Laird, N.M., Rubin, D.B., 1977. Maximum likelihood from incomplete data via the em algorithm. *Journal of the Royal Statistical Society: Series B (Methodological)* 39, 1–22. URL: <https://rss.onlinelibrary.wiley.com/doi/abs/10.1111/j.2517-6161.1977.tb01600.x>, doi:<https://doi.org/10.1111/j.2517-6161.1977.tb01600.x>.

Dockès, J., Varoquaux, G., Poline, J.B., 2021. Preventing dataset shift from breaking machine-learning biomarkers. *GigaScience* 10, giab055.

Dubois, J., Alison, M., Counsell, S.J., Hertz-Pannier, L., Hüppi, P.S., Benders, M.J., 2020. MRI of the neonatal brain: A review of methodological challenges and neuroscientific advances. *Journal of Magnetic Resonance Imaging* 53, 1318–1343. URL: <http://dx.doi.org/10.1002/jmri.27192>, doi:10.1002/jmri.27192.

Ebner, M., Wang, G., Li, W., Aertsen, M., Patel, P.A., Aughwane, R., Melbourne, A., Doel, T., Dymarkowski, S., De Coppi, P., et al., 2020. An automated framework for localization, segmentation and super-resolution reconstruction of fetal brain mri. *NeuroImage* 206, 116324.

Edwards, A.D., Rueckert, D., Smith, S.M., Abo Seada, S., Alansary, A., Almalbis, J., Allsop, J., Andersson, J., Arichi, T., Arulkumaran, S., Bastiani, M., Batalle, D., Baxter, L., Bozek, J., Braithwaite, E., Brandon, J., Carney, O., Chew, A., Christiaens, D., Chung, R., Colford, K., Cordero-Grande, L., Counsell, S.J., Cullen, H., Cupitt, J., Curtis, C., Davidson, A., Deprez, M., Dillon, L., Dimitrakopoulou, K., Dimitrova, R., Duff, E.,

- Falconer, S., Farahibozorg, S.R., Fitzgibbon, S.P., Gao, J., Gaspar, A., Harper, N., Harrison, S.J., Hughes, E.J., Hutter, J., Jenkinson, M., Jbabdi, S., Jones, E., Karolis, V., Kyriakopoulou, V., Lenz, G., Makropoulos, A., Malik, S., Mason, L., Mortari, F., Nosarti, C., Nunes, R.G., O’Keeffe, C., O’Muirheartaigh, J., Patel, H., Passerat-Palmbach, J., Pietsch, M., Price, A.N., Robinson, E.C., Rutherford, M.A., Schuh, A., Sotiropoulos, S., Steinweg, J., Teixeira, R.P.A.G., Tenev, T., Tournier, J.D., Tusor, N., Uus, A., Vecchiato, K., Williams, L.Z.J., Wright, R., Wurie, J., Hajnal, J.V., 2022. The developing human connectome project neonatal data release. *Frontiers in Neuroscience* 16. URL: <http://dx.doi.org/10.3389/fnins.2022.886772>, doi:10.3389/fnins.2022.886772.
- Frid-Adar, M., Diamant, I., Klang, E., Amitai, M., Goldberger, J., Greenspan, H., 2018. Gan-based synthetic medical image augmentation for increased cnn performance in liver lesion classification. *Neurocomputing* 321, 321–331. doi:10.1016/j.neucom.2018.09.013.
- Gagnon-Audet, J.C., Monti, R.P., Schwab, D.J., 2023. AWE: Adaptive weight-space ensembling for few-shot fine-tuning, in: *ICLR 2023 Workshop on Mathematical and Empirical Understanding of Foundation Models*. URL: <https://openreview.net/forum?id=rrMIPIboZL>.
- Garel, C., Garel, C., 2004. *MRI of the Fetal Brain*. Springer.
- Gholipour, A., Estroff, J.A., Warfield, S.K., 2010. Robust super-resolution volume reconstruction from slice acquisitions: application to fetal brain mri. *IEEE transactions on medical imaging* 29, 1739–1758.
- Glenn, O., Barkovich, A., 2006. Magnetic resonance imaging of the fetal brain and spine: An increasingly important tool in prenatal diagnosis, part 1. *American Journal of Neuroradiology* 27, 1604–1611. URL: <https://www.ajnr.org/content/27/8/1604>, arXiv:<https://www.ajnr.org/content/27/8/1604.full.pdf>.
- Gopinath, K., Hoopes, A., Alexander, D.C., Arnold, S.E., Balbastre, Y., Casamitjana, A., Cheng, Y., Chua, R.Y.Z., Edlow, B.L., Fischl, B., et al., 2024. Synthetic data in generalizable, learning-based neuroimaging. *Imaging Neuroscience* .

- Guan, H., Liu, M., 2022. Domain adaptation for medical image analysis: A survey. *IEEE Transactions on Biomedical Engineering* 69, 1173–1185. URL: <http://dx.doi.org/10.1109/TBME.2021.3117407>, doi:10.1109/tbme.2021.3117407.
- Halfon, N., Larson, K., Lu, M., Tullis, E., Russ, S., 2014. Lifecourse health development: past, present and future. *Matern. Child Health J.* 18, 344–365.
- Hu, F., Chen, A.A., Horng, H., Bashyam, V., Davatzikos, C., Alexander-Bloch, A., Li, M., Shou, H., Satterthwaite, T.D., Yu, M., Shinohara, R.T., 2023. Image harmonization: A review of statistical and deep learning methods for removing batch effects and evaluation metrics for effective harmonization. *NeuroImage* 274, 120125. URL: <https://www.sciencedirect.com/science/article/pii/S1053811923002719>, doi:<https://doi.org/10.1016/j.neuroimage.2023.120125>.
- Huang, X., Liu, Y., Li, Y., Qi, K., Gao, A., Zheng, B., Liang, D., Long, X., 2023. Deep learning-based multiclass brain tissue segmentation in fetal mris. *Sensors* 23. URL: <https://www.mdpi.com/1424-8220/23/2/655>, doi:10.3390/s23020655.
- Jakab, A., Payette, K., Mazzone, L., Schauer, S., Muller, C.O., Kottke, R., Ochsenbein-Kölble, N., Tuura, R., Moehrlen, U., Meuli, M., 2021. Emerging magnetic resonance imaging techniques in open spina bifida in utero. *European Radiology Experimental* 5. URL: <http://dx.doi.org/10.1186/s41747-021-00219-z>, doi:10.1186/s41747-021-00219-z.
- Kaandorp, M.P.T., Agbelese, D., Asma-ull, H., Kim, H.G., Payette, K., Grehten, P., Giulio, G.A., Láncki, L.I., Jakab, A., 2025. Pathological mri segmentation by synthetic pathological data generation in fetuses and neonates. URL: <https://arxiv.org/abs/2501.19338>, arXiv:2501.19338.
- Karani, N., Chaitanya, K., Baumgartner, C., Konukoglu, E., 2018. A lifelong learning approach to brain mr segmentation across scanners and protocols, in: Frangi, A.F., Schnabel, J.A., Davatzikos, C., Alberola-López, C., Fichtinger, G. (Eds.), *Medical Image Computing and Computer Assisted Intervention – MICCAI 2018*, Springer International Publishing, Cham. pp. 476–484.

- Karolis, V.R., Cordero-Grande, L., Price, A.N., Hughes, E., Fitzgibbon, S.P., Kyriakopoulou, V., Uus, A., Harper, N., Prokopenko, D., Bridglal, D., et al., 2025. The developing human connectome project fetal functional mri release: Methods and data structures. *Imaging Neuroscience* 3, imag-a_00512.
- Kazeminiya, S., Baur, C., Kuijper, A., van Ginneken, B., Navab, N., Albarqouni, S., Mukhopadhyay, A., 2020. Gans for medical image analysis. *Artificial Intelligence in Medicine* 109, 101938. URL: <https://www.sciencedirect.com/science/article/pii/S0933365719311510>, doi:<https://doi.org/10.1016/j.artmed.2020.101938>.
- Kazerouni, A., Aghdam, E.K., Heidari, M., Azad, R., Fayyaz, M., Hachililoglu, I., Merhof, D., 2023. Diffusion models in medical imaging: A comprehensive survey. *Medical Image Analysis* 88, 102846. URL: <https://www.sciencedirect.com/science/article/pii/S1361841523001068>, doi:<https://doi.org/10.1016/j.media.2023.102846>.
- Kebiri, H., Canales-Rodríguez, E.J., Lajous, H., de Dumast, P., Girard, G., Alemán-Gómez, Y., Koob, M., Jakab, A., Bach Cuadra, M., 2022. Through-plane super-resolution with autoencoders in diffusion magnetic resonance imaging of the developing human brain. *Frontiers in Neurology* 13, 827816.
- Kelley, W., Ngo, N., Dalca, A.V., Fischl, B., Zöllei, L., Hoffmann, M., 2024. Boosting skull-stripping performance for pediatric brain images. URL: <https://arxiv.org/abs/2402.16634>, doi:10.48550/ARXIV.2402.16634.
- Khosravi, B., Li, F., Dapamede, T., Rouzrokh, P., Gamble, C.U., Trivedi, H.M., Wyles, C., Selligren, A., Purkayastha, S., Erickson, B., Gichoya, J., 2023. Synthetically enhanced: Unveiling synthetic data’s potential in medical imaging research. *ArXiv abs/2311.09402*. doi:10.48550/arXiv.2311.09402.
- Kirkpatrick, J., Pascanu, R., Rabinowitz, N., Veness, J., Desjardins, G., Rusu, A.A., Milan, K., Quan, J., Ramalho, T., Grabska-Barwinska, A., et al., 2017. Overcoming catastrophic forgetting in neural networks. *Proceedings of the national academy of sciences* 114, 3521–3526.

- Kuklisova-Murgasova, M., Quaghebeur, G., Rutherford, M.A., Hajnal, J.V., Schnabel, J.A., 2012. Reconstruction of fetal brain MRI with intensity matching and complete outlier removal. *Medical image analysis* 16, 1550–1564.
- Kumar, A., Raghunathan, A., Jones, R.M., Ma, T., Liang, P., 2022. Fine-tuning can distort pretrained features and underperform out-of-distribution, in: *International Conference on Learning Representations*. URL: <https://openreview.net/forum?id=UYneFzXSJWh>.
- Kyriakopoulou, V., Vatansever, D., Davidson, A., Patkee, P., Elkommos, S., Chew, A., Martinez-Biarge, M., Hagberg, B., Damodaram, M., Allsop, J., et al., 2017. Normative biometry of the fetal brain using magnetic resonance imaging. *Brain Structure and Function* 222, 2295–2307.
- Lajous, H., Boeuf Fló, A.I., Gordaliza, P.M., Esteban, O., Marqués, F., Dunet, V., Koob, M., Cuadra, M.B., 2024a. Maturation-informed synthetic magnetic resonance images of the developing human fetal brain. *bioRxiv* URL: <https://www.biorxiv.org/content/early/2024/04/09/2024.04.08.588566>, doi:10.1101/2024.04.08.588566.
- Lajous, H., le Boeuf Fló, A., Esteban, O., Bach Cuadra, M., 2024b. Dataset Maturation-informed Synthetic Magnetic Resonance Images of the Developing Human Fetal Brain. URL: <https://doi.org/10.5281/zenodo.10940427>, doi:10.5281/zenodo.10940427.
- Lajous, H., Roy, C.W., Hilbert, T., de Dumast, P., Tourbier, S., Alemán-Gómez, Y., Yerly, J., Yu, T., Kebiri, H., Payette, K., Ledoux, J.B., Meuli, R., Hagmann, P., Jakab, A., Dunet, V., Koob, M., Kober, T., Stuber, M., Bach Cuadra, M., 2022. A fetal brain magnetic resonance acquisition numerical phantom (fabian). *Scientific Reports* 12. URL: <http://dx.doi.org/10.1038/s41598-022-10335-4>, doi:10.1038/s41598-022-10335-4.
- Lhermitte, E., Dinomais, M., Oyaneder, R.A., Bleyenheuft, Y., Guzzetta, A., Brochard, S., Rousseau, F., 2024. Validating stroke lesion segmentation methods using mri in children: transferability of deep learning models, in: *ISBI 2024-21st IEEE International Symposium on Biomedical Imaging*.

- Li, D., Yang, Y., Song, Y.Z., Hospedales, T.M., 2018. Learning to generalize: meta-learning for domain generalization, in: Proceedings of the Thirty-Second AAAI Conference on Artificial Intelligence and Thirtieth Innovative Applications of Artificial Intelligence Conference and Eighth AAAI Symposium on Educational Advances in Artificial Intelligence, AAAI Press.
- Li, H., Li, H., Zhao, W., Fu, H., Su, X., Hu, Y., Liu, J., 2023. Frequency-mixed single-source domain generalization for medical image segmentation, in: Greenspan, H., Madabhushi, A., Mousavi, P., Salcudean, S., Duncan, J., Syeda-Mahmood, T., Taylor, R. (Eds.), Medical Image Computing and Computer Assisted Intervention – MICCAI 2023, Springer Nature Switzerland, Cham. pp. 127–136.
- Liu, P., Puonti, O., Hu, X., Alexander, D.C., Iglesias, J.E., 2024a. Brain-id: Learning contrast-agnostic anatomical representations for brain imaging, in: European Conference on Computer Vision (ECCV).
- Liu, P., Puonti, O., Sorby-Adams, A., Kimberly, W.T., Iglesias, J.E., 2024b. Pepsi: Pathology-enhanced pulse-sequence-invariant representations for brain mri. URL: <https://arxiv.org/abs/2403.06227>, doi:10.48550/ARXIV.2403.06227.
- Liu, Q., Chen, C., Dou, Q., Heng, P.A., 2022. Single-domain generalization in medical image segmentation via test-time adaptation from shape dictionary. Proc. Conf. AAAI Artif. Intell. 36, 1756–1764.
- Loizillon, S., Bottani, S., Maire, A., Ströer, S., Dormont, D., Colliot, O., Burgos, N., 2023. Transfer learning from synthetic to routine clinical data for motion artefact detection in brain t1-weighted mri, in: Medical Imaging 2023: Image Processing, SPIE. pp. 343–349.
- Machado-Rivas, F., Gandhi, J., Choi, J.J., Velasco-Annis, C., Afacan, O., Warfield, S.K., Gholipour, A., Jaimes, C., 2022. Normal growth, sexual dimorphism, and lateral asymmetries at fetal brain mri. Radiology 303, 162–170. URL: <https://doi.org/10.1148/radiol.211222>, doi:10.1148/radiol.211222, arXiv:<https://doi.org/10.1148/radiol.211222>. PMID: 34931857.

- Makropoulos, A., Robinson, E.C., Schuh, A., Wright, R., Fitzgibbon, S., Bozek, J., Counsell, S.J., Steinweg, J., Passerat-Palmbach, J., Lenz, G., Mortari, F., Tenev, T., Duff, E.P., Bastiani, M., Cordero-Grande, L., Hughes, E., Tusor, N., Tournier, J.D., Hutter, J., Price, A.N., Murgasova, M., Kelly, C., Rutherford, M.A., Smith, S.M., Edwards, A.D., Hajnal, J.V., Jenkinson, M., Rueckert, D., 2017. The developing human connectome project: a minimal processing pipeline for neonatal cortical surface reconstruction. *bioRxiv* URL: <https://www.biorxiv.org/content/early/2017/04/07/125526>, doi:10.1101/125526, arXiv:<https://www.biorxiv.org/content/early/2017/04/07/125526.full.pdf>.
- Makropoulos, A., Robinson, E.C., Schuh, A., Wright, R., Fitzgibbon, S., Bozek, J., Counsell, S.J., Steinweg, J., Vecchiato, K., Passerat-Palmbach, J., Lenz, G., Mortari, F., Tenev, T., Duff, E.P., Bastiani, M., Cordero-Grande, L., Hughes, E., Tusor, N., Tournier, J.D., Hutter, J., Price, A.N., Teixeira, R.P.A., Murgasova, M., Victor, S., Kelly, C., Rutherford, M.A., Smith, S.M., Edwards, A.D., Hajnal, J.V., Jenkinson, M., Rueckert, D., 2018. The developing human connectome project: A minimal processing pipeline for neonatal cortical surface reconstruction. *NeuroImage* 173, 88–112. URL: <https://www.sciencedirect.com/science/article/pii/S1053811918300545>, doi:<https://doi.org/10.1016/j.neuroimage.2018.01.054>.
- Niemeijer, J., Schwonberg, M., Termöhlen, J.A., Schmidt, N.M., Fingscheidt, T., 2024. Generalization by adaptation: Diffusion-based domain extension for domain-generalized semantic segmentation, in: *Proceedings of the IEEE/CVF Winter Conference on Applications of Computer Vision*, pp. 2830–2840.
- Omidi, A., Shamaei, A., Verschuu, A., King, R., Leijser, L., Souza, R., 2024. Unsupervised domain adaptation of brain MRI skull stripping trained on adult data to newborns: Combining synthetic data with domain invariant features, in: *Medical Imaging with Deep Learning*. URL: <https://openreview.net/forum?id=vu4LsiSpf7>.
- Ortiz-Jimenez, G., Favero, A., Frossard, P., 2023. Task arithmetic in the tangent space: Improved editing of pre-trained models. *Advances in Neural Information Processing Systems* 36, 66727–66754.

- Ouyang, C., Chen, C., Li, S., Li, Z., Qin, C., Bai, W., Rueckert, D., 2022. Causality-inspired single-source domain generalization for medical image segmentation. *IEEE Transactions on Medical Imaging* 42, 1095–1106.
- Paprocki, A., Salvado, O., Fookes, C., 2024. Synthetic data for deep learning in computer vision & medical imaging: A means to reduce data bias. *ACM Comput. Surv.* URL: <https://doi.org/10.1145/3663759>, doi:10.1145/3663759. just Accepted.
- Paszke, A., Gross, S., Massa, F., Lerer, A., Bradbury, J., Chanan, G., Killeen, T., Lin, Z., Gimelshein, N., Antiga, L., et al., 2019. Pytorch: An imperative style, high-performance deep learning library. *Advances in neural information processing systems* 32.
- Payette, K., de Dumast, P., Kebiri, H., Ezhov, I., Paetzold, J., Shit, S., Iqbal, A., Khan, R., Kottke, R., Grehten, P., Ji, H., Lanczi, L., Nagy, M., Beresova, M., Nguyen, T., Natalucci, G., Karayannis, T., Menze, B., Bach Cuadra, M., Jakab, A., 2021. An automatic multi-tissue human fetal brain segmentation benchmark using the fetal tissue annotation dataset. *Scientific Data* 8. doi:10.1038/s41597-021-00946-3.
- Payette, K., Jakab, A., 2021. Fetal tissue annotation dataset. URL: <https://repo-prod.prod.sagebase.org/repo/v1/doi/locate?id=syn23747212&type=ENTITY>, doi:10.7303/SYN23747212.
- Payette, K., Li, H.B., de Dumast, P., Licandro, R., Ji, H., Siddiquee, M.M.R., Xu, D., Myronenko, A., Liu, H., Pei, Y., et al., 2023. Fetal brain tissue annotation and segmentation challenge results. *Medical Image Analysis* 88, 102833.
- Payette, K., Steger, C., Licandro, R., de Dumast, P., Li, H.B., Barkovich, M., Li, L., Dannecker, M., Chen, C., Ouyang, C., McConnell, N., Miron, A., Li, Y., Uus, A., Grigorescu, I., Gilliland, P.R., Siddiquee, M.M.R., Xu, D., Myronenko, A., Wang, H., Huang, Z., Ye, J., Alenyà, M., Comte, V., Camara, O., Masson, J.B., Nilsson, A., Godard, C., Mazher, M., Qayyum, A., Gao, Y., Zhou, H., Gao, S., Fu, J., Dong, G., Wang, G., Rieu, Z., Yang, H., Lee, M., Plotka, S., Grzeszczyk, M.K., Sitek, A., Daza, L.V., Usma, S., Arbelaez, P., Lu, W., Zhang, W., Liang, J., Valabregue, R., Joshi, A.A., Nayak, K.N., Leahy, R.M., Wilhelmi, L., Dändliker, A., Ji, H., Gennari, A.G., Jakovčić, A., Klaić, M., Adžić, A., Marković, P., Grabarić,

- G., Kasprian, G., Dovjak, G., Rados, M., Vasung, L., Cuadra, M.B., Jakab, A., 2024a. Multi-center fetal brain tissue annotation (feta) challenge 2022 results. *arXiv:2402.09463*.
- Payette, K., Steger, C., Licandro, R., de Dumast, P., Li, H.B., Barkovich, M., Li, L., Dannecker, M., Chen, C., Ouyang, C., et al., 2024b. Multi-center fetal brain tissue annotation (feta) challenge 2022 results. *arXiv preprint arXiv:2402.09463*.
- Pfeifer, C.M., Willard, S.D., Cornejo, P., 2019. Mri depiction of fetal brain abnormalities. *Acta Radiologica Open* 8, 205846011989498. URL: <http://dx.doi.org/10.1177/2058460119894987>, doi:10.1177/2058460119894987.
- Price, A.N., Cordero-Grande, L., Hughes, E., Hiscocks, S., Green, E., McCabe, L., Hutter, J., Ferrazzi, G., Deprez, M., Roberts, T., et al., 2019. The developing human connectome project (dhcp): fetal acquisition protocol, in: *Proceedings of the annual meeting of the International Society of Magnetic Resonance in Medicine (ISMRM), International Society for Magnetic Resonance in Medicine (ISMRM)*.
- Ramé, A., Ahuja, K., Zhang, J., Cord, M., Bottou, L., Lopez-Paz, D., 2023. Model ratatouille: Recycling diverse models for out-of-distribution generalization, in: *International Conference on Machine Learning*, PMLR. pp. 28656–28679.
- Rame, A., Kirchmeyer, M., Rahier, T., Rakotomamonjy, A., Gallinari, P., Cord, M., 2022. Diverse weight averaging for out-of-distribution generalization. *Advances in Neural Information Processing Systems* 35, 10821–10836.
- Rousseau, F., Kim, K., Studholme, C., Koob, M., Dietemann, J.L., 2010. On Super-Resolution for Fetal Brain MRI. *Springer Berlin Heidelberg*. p. 355–362. URL: http://dx.doi.org/10.1007/978-3-642-15745-5_44, doi:10.1007/978-3-642-15745-5_44.
- Saleem, S.N., 2014. Fetal mri: An approach to practice: A review. *Journal of Advanced Research* 5, 507–523. URL: <https://www.sciencedirect.com/science/article/pii/S2090123213000805>, doi:<https://doi.org/10.1016/j.jare.2013.06.001>.

- Sanchez, T., Esteban, O., Gomez, Y., Pron, A., Koob, M., Dunet, V., Girard, N., Jakab, A., Eixarch, E., Auzias, G., et al., 2024. Fetmrqc: A robust quality control system for multi-centric fetal brain mri. *Medical Image Analysis* , 103282.
- Shang, Z., Turja, M.A., Feczko, E., Houghton, A., Rueter, A., Moore, L.A., Snider, K., Hendrickson, T., Reiners, P., Stoyell, S., et al., 2022. Learning strategies for contrast-agnostic segmentation via synthseg for infant mri data, in: *International Conference on Medical Imaging with Deep Learning*, PMLR. pp. 1075–1084.
- Shen, L., Zheng, J., Lee, E.H., Shpanskaya, K., McKenna, E.S., Atluri, M.G., Plasto, D., Mitchell, C., Lai, L.M., Guimaraes, C.V., Dahmouh, H., Chueh, J., Halabi, S.S., Pauly, J.M., Xing, L., Lu, Q., Oztekin, O., Kline-Fath, B.M., Yeom, K.W., 2022. Attention-guided deep learning for gestational age prediction using fetal brain mri. *Scientific Reports* 12. URL: <http://dx.doi.org/10.1038/s41598-022-05468-5>, doi:10.1038/s41598-022-05468-5.
- Shorten, C., Khoshgoftaar, T.M., 2019. A survey on image data augmentation for deep learning. *Journal of big data* 6, 1–48.
- Stiles, J., Jernigan, T.L., 2010. The basics of brain development. *Neuropsychology Review* 20, 327–348. URL: <http://dx.doi.org/10.1007/s11065-010-9148-4>, doi:10.1007/s11065-010-9148-4.
- Stojanovski, Z., Roth, K., Akata, Z., 2022. Momentum-based weight interpolation of strong zero-shot models for continual learning. *ArXiv abs/2211.03186*. doi:10.48550/arXiv.2211.03186.
- Thambawita, V.L., Salehi, P., Sheshkal, S.A., Hicks, S., L.Hammer, H., Parasa, S., Lange, T., Halvorsen, P., Riegler, M., 2021. Singan-seg: Synthetic training data generation for medical image segmentation. *PLoS ONE* 17. doi:10.1371/journal.pone.0267976.
- Tobin, J., Fong, R., Ray, A., Schneider, J., Zaremba, W., Abbeel, P., 2017. Domain randomization for transferring deep neural networks from simulation to the real world, in: *2017 IEEE/RSJ international conference on intelligent robots and systems (IROS)*, IEEE. pp. 23–30.

- Tourbier, S., Bresson, X., Hagmann, P., Thiran, J.P., Meuli, R., Cuadra, M.B., 2015. An efficient total variation algorithm for super-resolution in fetal brain mri with adaptive regularization. *NeuroImage* 118, 584–597.
- Uus, A.U., Kyriakopoulou, V., Makropoulos, A., Fukami-Gartner, A., Cromb, D., Davidson, A., Cordero-Grande, L., Price, A.N., Grigorescu, I., Williams, L.Z.J., Robinson, E.C., Lloyd, D., Pushparajah, K., Story, L., Hutter, J., Counsell, S.J., Edwards, A.D., Rutherford, M.A., Hajnal, J.V., Deprez, M., 2023. Bounti: Brain volumetry and automated parcellation for 3d fetal mri. *bioRxiv* URL: <https://www.biorxiv.org/content/early/2023/04/27/2023.04.18.537347>, doi:10.1101/2023.04.18.537347.
- Valabregue, R., Girka, F., Pron, A., Rousseau, F., Auzias, G., 2024. Comprehensive analysis of synthetic learning applied to neonatal brain mri segmentation. *Human Brain Mapping* 45, e26674.
- Varoquaux, G., Cheplygina, V., 2022. Machine learning for medical imaging: methodological failures and recommendations for the future. *NPJ digital medicine* 5, 48.
- Wang, Z., Jiang, Y., Zheng, H., Wang, P., He, P., Wang, Z., Chen, W., Zhou, M., et al., 2023. Patch diffusion: Faster and more data-efficient training of diffusion models. *Advances in neural information processing systems* 36, 72137–72154.
- Wortsman, M., Ilharco, G., Gadre, S.Y., Roelofs, R., Gontijo-Lopes, R., Morcos, A.S., Namkoong, H., Farhadi, A., Carmon, Y., Kornblith, S., et al., 2022a. Model soups: averaging weights of multiple fine-tuned models improves accuracy without increasing inference time, in: *International conference on machine learning*, PMLR. pp. 23965–23998.
- Wortsman, M., Ilharco, G., Kim, J.W., Li, M., Kornblith, S., Roelofs, R., Lopes, R.G., Hajishirzi, H., Farhadi, A., Namkoong, H., et al., 2022b. Robust fine-tuning of zero-shot models, in: *Proceedings of the IEEE/CVF conference on computer vision and pattern recognition*, pp. 7959–7971.
- Xu, J., Moyer, D., Gagoski, B., Iglesias, J.E., Grant, P.E., Golland, P., Adalsteinsson, E., 2023. NeSVoR: Implicit neural representation for slice-to-volume reconstruction in MRI. *IEEE Transactions on Medical Imaging*.

- Xu, X., Sun, C., Yu, H., Yan, G., Zhu, Q., Kong, X., Pan, Y., Xu, H., Zheng, T., Zhou, C., Wang, Y., Xiao, J., Chen, R., Li, M., Zhang, S., Hu, H., Zou, Y., Wang, J., Wang, G., Wu, D., 2024. Site effects in multisite fetal brain mri: morphological insights into early brain development. *European Radiology* URL: <http://dx.doi.org/10.1007/s00330-024-11084-w>, doi:10.1007/s00330-024-11084-w.
- Xu, Y., Xie, S., Reynolds, M., Ragoza, M., Gong, M., Batmanghelich, K., 2022. Adversarial Consistency for Single Domain Generalization in Medical Image Segmentation. Springer Nature Switzerland. p. 671–681. URL: http://dx.doi.org/10.1007/978-3-031-16449-1_64, doi:10.1007/978-3-031-16449-1_64.
- Yadav, P., Tam, D., Choshen, L., Raffel, C.A., Bansal, M., 2024. Ties-merging: Resolving interference when merging models. *Advances in Neural Information Processing Systems* 36.
- Yan, W., Huang, L., Xia, L., Gu, S., Yan, F., Wang, Y., Tao, Q., 2020. Mri manufacturer shift and adaptation: Increasing the generalizability of deep learning segmentation for mr images acquired with different scanners. *Radiology: Artificial Intelligence* 2, e190195. URL: <http://dx.doi.org/10.1148/ryai.2020190195>, doi:10.1148/ryai.2020190195.
- Zalevskiy, V., Sanchez, T., Kaandorp, M., Roulet, M., Fajardo-Rojas, D., Li, L., Hutter, J., Li, H.B., Barkovich, M., Ji, H., Wilhelmi, L., Dändliker, A., Steger, C., Koob, M., Gomez, Y., Jakovčić, A., Klaić, M., Adžić, A., Marković, P., Grabarić, G., Rados, M., Verdera, J.A., Kasprian, G., Dobjak, G., Gaubert-Rachmühl, R., Aschwanden, M., Zeng, Q., Karimi, D., Peruzzo, D., Ciceri, T., Longari, G., Hamadache, R.E., Bouzid, A., Lladó, X., Chiarella, S., Martí-Juan, G., Ángel González Ballester, M., Castellaro, M., Pinamonti, M., Visani, V., Cremese, R., Sam, K., Gaudfernau, F., Ahir, P., Parikh, M., Zenk, M., Baumgartner, M., Maier-Hein, K., Tianhong, L., Hong, Y., Longfei, Z., Preloznik, D., Žiga Špiclin, Choi, J.W., Li, M., Fu, J., Wang, G., Jiang, J., Tong, L., Du, B., Gondova, A., You, S., Im, K., Qayyum, A., Mazher, M., Niederer, S.A., Jakab, A., Licandro, R., Payette, K., Cuadra, M.B., 2025. Advances in automated fetal brain mri segmentation and biometry: Insights from the feta 2024 challenge. URL: <https://arxiv.org/abs/2505.02784>, arXiv:2505.02784.

- Zalevskyi, V., Sanchez, T., Roulet, M., Aviles Verdera, J., Hutter, J., Kebiri, H., Bach Cuadra, M., 2024. Improving cross-domain brain tissue segmentation in fetal mri with synthetic data, in: Linguraru, M.G., Dou, Q., Feragen, A., Giannarou, S., Glocker, B., Lekadir, K., Schnabel, J.A. (Eds.), Medical Image Computing and Computer Assisted Intervention – MICCAI 2024, Springer Nature Switzerland, Cham. pp. 437–447.
- Zhou, K., Liu, Z., Qiao, Y., Xiang, T., Loy, C.C., 2023. Domain generalization: A survey. *IEEE Transactions on Pattern Analysis and Machine Intelligence* 45, 4396–4415. doi:10.1109/TPAMI.2022.3195549.
- Zhou, K., Yang, Y., Qiao, Y., Xiang, T., 2021. Domain generalization with mixstyle, in: International Conference on Learning Representations. URL: <https://openreview.net/forum?id=6xHJ37MVxxp>.

Supplementary material

A1: Ablation on data augmentations

In this additional experiment, we compared the **SynthSeg**-based augmentations to a common set of augmentations from MONAI (referred to as *simple aug.*). We re-trained the models using the following augmentations, each applied with a random probability of 0.5: random affine deformation (rotation=0.2, scale=0.1, translate=30, sheer=0.1), random contrast change (Gamma transformation) ($\gamma \in [0.5, 1.5]$), random Gaussian noise ($\mu = 0, \sigma = 0.1$), random blurring ($\sigma \in [0.5, 1.5]$), and scaling to the 0-1 range. Compared to these *simple aug.*, **SynthSeg**-based augmentation has three additional components: a random non-linear deformation, random bias field, and a random resampling simulating an acquisition at a different resolution.

The results in Table S1 show a different picture than the results in the main paper. When comparing models trained using simple augmentations, the model trained using real data outperforms **FetalSynthSeg** (69.9 vs 66.9 Dice). Moving from simple augmentation increases the performance of all methods considered: **FaBiAN** (+2.9), **randFaBiAN** (+3.9), **FetalSynthSeg** (+8.0), **Real Data** (+1.9). This illustrates clearly how these data augmentation strategies are instrumental to the performance of **FetalSynthSeg**. They are also strong contenders for a model trained on real data and could be used in the future. A detailed ablation study of augmentations would be an interesting future step.

Table S1: Mean Dice for models trained on different sources of data. The variance is computed over all testing subjects within a split. The best performing method is shown in **boldface** in each column, and the second best is underlined.

Augmentation type	Testing split	CHUV-mial		KISPI-irtk		KISPI-mial		Global
	Training split	KISPI-irtk	KISPI-mial	CHUV-mial	KISPI-mial	CHUV-mial	KISPI-irtk	
Simple	FaBiAN	66.9 ± 5.1	70.3 ± 6.9	51.6 ± 14.1	56.7 ± 14.2	59.8 ± 15.2	57.3 ± 17.9	60.4 ± 14.3
	randFaBiAN	74.1 ± 3.1	69.0 ± 6.4	63.8 ± 10.3	54.0 ± 9.3	62.0 ± 13.8	62.8 ± 13.0	64.3 ± 12.1
	FetalSynthSeg	72.9 ± 4.0	70.3 ± 6.2	71.4 ± 9.3	68.3 ± 8.2	58.7 ± 15.5	60.0 ± 16.1	66.9 ± 11.8
SynthSeg	FaBiAN	74.2 ± 4.2	73.1 ± 5.7	53.6 ± 13.3	56.6 ± 12.9	60.6 ± 17.1	61.5 ± 20.1	63.3 ± 15.5
	randFaBiAN	<u>79.1 ± 2.3</u>	<u>78.2 ± 2.9</u>	55.1 ± 12.7	68.9 ± 7.8	60.7 ± 7.3	<u>68.1 ± 14.7</u>	68.3 ± 13.8
	SynthSeg	75.9 ± 3.9	73.7 ± 3.9	<u>70.9 ± 9.2</u>	<u>74.8 ± 7.8</u>	60.5 ± 15.7	63.4 ± 16.8	72.2 ± 13.0
	FetalSynthSeg	80.7 ± 2.0	76.9 ± 3.3	79.2 ± 9.0	76.8 ± 6.9	<u>67.5 ± 16.0</u>	68.5 ± 15.6	74.9 ± 11.5
Simple	Real Data	76.5 ± 3.2	75.2 ± 3.5	69.6 ± 13.6	67.7 ± 12.9	67.2 ± 17.6	63.4 ± 17.0	69.9 ± 12.6
SynthSeg	Real Data	77.2 ± 4.0	78.5 ± 3.3	70.6 ± 13.9	71.9 ± 11.5	68.0 ± 19.3	64.3 ± 19.1	<u>71.8 ± 13.9</u>

A2: Comparing *FaBiAN* vs *FetalSynthSeg* on the same number of images

To ensure a fair comparison between *FaBiAN* and *FetalSynthSeg* we equalize the computational budget used to generate images for these two approaches. We generate offline 6000 synthetic images per split, as in our *FaBiAN* experiments, and use them to train a *FetalSynthSeg*-6k model. Table S2 shows that although this model achieves slightly lower results than *FetalSynthSeg*, it follows similar trends in performance across splits and still outperforms even the *randFaBiAN* approach overall (average Dice of *FetalSynthSeg*-6k 72.2 ± 8.8 is vs average Dice of *randFaBiAN* of 68.3 ± 8.5 across all splits).

Table S2: Dice scores comparing *FetalSynthSeg* model trained on the same amount of synthetic images as *FaBiAN* models.

Testing Split	CHUV-mial		KISPI-irtk		KISPI-mial		Global
Training Split	KISPI-irtk	KISPI-mial	CHUV-mial	KISPI-mial	CHUV-mial	KISPI-irtk	
<i>FaBiAN</i>	74.2 ± 4.2	73.1 ± 5.7	53.6 ± 13.3	56.6 ± 12.9	60.6 ± 17.1	61.5 ± 20.1	63.3 ± 15.5
<i>randFaBiAN</i>	79.1 ± 2.3	78.2 ± 2.9	55.1 ± 12.7	68.9 ± 7.8	60.7 ± 7.3	68.1 ± 14.7	68.3 ± 13.8
<i>FetalSynthSeg</i> -6k	79.0 ± 2.6	76.0 ± 3.6	78.3 ± 9.2	75.1 ± 6.6	66.5 ± 15.9	67.7 ± 15.4	72.2 ± 13.0
<i>FetalSynthSeg</i>	80.7 ± 2.0	76.9 ± 3.3	79.2 ± 9.0	76.8 ± 6.9	67.5 ± 16.0	68.5 ± 15.6	74.9 ± 11.5

A3: Generation parameters

In the Table S3 we report parameters used to create synthetic images with the *FaBiAN* generator.

A4: Additional quantitative results

We present additional quantitative results related to the conducted experiments, reporting the Dice scores per tissue for all of the tested models in Tables S4 as well as the average 95th-percentile Hausdorff distance score in Table S5.

A5: Out-of-domain evaluation and SoTA comparison

Tables S6 and S7 present the HD95 metrics and label-wise performance comparing *cesne-digair* with the *FetalSynthSeg*, *FetalSynthSeg*-FT, and *DRIFTS* across the OOD testing testing splits.

We note that, while there is no single model that consistently outperforms others in terms of HD95 across all test sets, each of our synthetic models—*FetalSynthSeg*, *FetalSynthSeg*-FT, and *DRIFTS* —achieves the best

Contrast	
Effective echo time (ms)	[90,300]
Echo spacing (ms)	6.12
Echo train length	150
Excitation flip angle (°)	90
Refocusing pulse flip angle (°)	[150,180]
Geometry	
Slice thickness (mm)	0.8
Slice gap (mm)	0
Number of slices	112
Phase oversampling (%)	80
Shift of field-of-view (mm)	0
Resolution	
Field-of-view (mm ²)	120x120
Base resolution (voxels)	150
Phase resolution (%)	70
Reconstruction matrix	150
Zero-interpolation filling	1
Acceleration technique	
Reference lines	42
Acceleration factor	2
Noise	
Mean	0
Standard deviation	<0.01

Table S3: FaBiAN Simulation Parameters for HASTE Imaging

performance on at least one dataset or modality. The optimal choice depends on the specific characteristics of the target domain. As demonstrated in our experiments, tuning the weight interpolation coefficient allows for a trade-off between generalization and domain-specific adaptation. Therefore, we recommend performing cross-validation on the target dataset to determine the most suitable domain randomization strategy and interpolation setting. Importantly, all of our domain-randomized models consistently outperform

Table S4: Mean and standard deviation of Dice score of the explored models for different testing and training splits. LV - lateral ventricles, CBM - cerebellum, SGM - sub-cortical gray matter, BS - brainstem, Mean DSC - value averaged across all segmentation labels.

Testing Splits	Training Split	Experiment	Mean DSC	CSF	GM	WM	LV	CBM	SGM	BS
CHUV-nial	KISPL-irrk	FetalSynthSeg	80.7± 2.0	79.3± 2.7	70.7± 3.6	86.4± 2.3	78.7 ± 5.4	88.5 ± 2.3	79.6± 5.4	81.9± 2.7
		Real data	77.2± 4.0	72.3± 7.1	68.4± 4.7	86.0± 2.8	75.8± 7.9	84.3± 9.2	76.4± 5.9	77.5± 4.7
		FaBiAN	74.2± 4.2	75.3± 4.2	64.2± 4.8	81.3± 4.4	71.9± 9.9	85.3± 3.6	62.8± 14.2	78.7± 3.3
		randFaBiAN	79.1± 2.3	77.0± 3.3	69.7± 3.6	85.9± 2.3	75.7± 5.3	87.4± 3.1	78.5± 8.4	79.5± 3.9
		SynthSeg	75.9± 3.9	73.7± 4.5	64.1± 6.3	83.1± 4.4	71.9± 8.5	85.8± 2.9	74.0± 10.6	78.8± 3.9
	KISPL-nial	FetalSynthSeg	76.9± 3.3	73.1± 8.1	60.5± 4.8	84.9± 3.0	77.3± 6.3	86.2± 4.3	83.7± 4.6	72.8± 3.9
		Real data	78.5± 3.3	79.0± 5.5	65.6± 4.4	85.8± 3.2	77.1± 7.3	86.5± 6.1	83.9± 3.8	71.4± 5.1
		FaBiAN	73.1± 5.7	73.3± 4.9	61.9± 5.9	81.1± 4.8	66.3± 10.6	81.0± 14.9	76.3± 7.3	71.5± 7.1
		randFaBiAN	78.2± 2.9	77.8± 3.9	64.1± 5.2	84.4± 3.2	75.5± 5.4	87.5± 4.6	83.0± 5.0	75.3± 5.0
		SynthSeg	73.7± 4.4	67.9± 12.0	55.1± 8.7	81.3± 4.2	72.1± 7.2	84.0± 3.0	80.9± 5.2	74.6± 3.9
	KISPL-irrk	FetalSynthSeg	79.2± 9.0	77.6± 10.9	69.4± 12.6	85.0± 12.9	79.7± 5.7	87.5± 9.1	74.8± 14.4	80.3± 6.6
		Real data	70.6± 13.9	58.6± 18.4	60.9± 15.9	84.8± 9.8	72.8± 11.7	74.3± 26.3	74.5± 11.0	68.1± 19.9
		FaBiAN	53.6± 13.3	51.4± 18.0	40.9± 11.9	74.9± 10.7	36.0± 13.8	45.9± 27.0	66.9± 12.1	59.0± 19.3
		randFaBiAN	55.1± 12.7	54.2± 17.2	41.5± 11.5	76.9± 10.5	37.2± 13.7	51.8± 28.0	66.5± 11.7	57.8± 18.5
		SynthSeg	70.9± 9.2	69.9± 11.6	58.6± 9.0	79.2± 11.8	66.4± 7.0	80.2± 11.3	68.8± 13.7	73.2± 9.2
		FetalSynthSeg	76.8± 6.9	78.7± 9.2	68.5± 9.1	86.5± 10.9	80.8± 4.7	85.1± 9.1	68.2± 12.3	69.9± 6.8
		Real data	71.9± 11.5	72.3± 19.5	65.3± 13.4	85.5± 7.6	71.6± 9.0	80.3± 20.2	64.8± 13.3	63.2± 14.5
		FaBiAN	56.6± 12.9	58.0± 17.6	39.3± 13.0	74.3± 9.5	50.6± 15.0	64.7± 27.7	58.7± 13.9	50.6± 18.7
		randFaBiAN	68.9± 7.8	60.8± 16.0	52.8± 11.1	82.2± 6.3	68.1± 9.7	80.1± 10.9	68.0± 12.3	70.2± 7.9
		SynthSeg	74.8± 7.8	74.4± 12.7	65.7± 10.8	85.4± 11.0	71.6± 7.3	86.3± 7.5	68.5± 13.1	72.0± 8.0
	KISPL-nial	FetalSynthSeg	67.5± 16.0	59.5± 28.3	48.7± 19.4	74.3± 17.3	78.6± 12.3	67.2± 29.7	79.3± 9.8	64.9± 16.0
		Real data	68.0± 19.3	62.1± 32.4	58.3± 15.7	81.8± 12.3	77.0± 14.5	64.6± 37.3	78.8± 9.9	53.4± 29.8
		FaBiAN	60.6± 17.1	52.9± 29.1	48.7± 15.2	77.6± 12.3	63.2± 17.3	53.7± 33.1	73.4± 14.5	54.8± 25.8
		randFaBiAN	60.7± 16.3	52.3± 28.6	49.6± 14.5	78.2± 12.4	63.7± 18.0	52.8± 32.5	73.8± 14.3	54.6± 22.4
		SynthSeg	60.5± 15.7	53.7± 26.0	43.8± 14.1	70.0± 15.4	65.9± 12.1	59.9± 28.5	71.1± 15.5	59.0± 17.0
		FetalSynthSeg	68.5± 15.6	63.2± 25.9	57.2± 16.8	82.1± 13.5	79.4± 12.2	73.2± 24.9	63.6± 18.4	60.8± 17.0
		Real data	64.3± 19.1	59.8± 29.0	55.0± 17.9	79.1± 15.5	72.6± 12.9	64.4± 33.8	62.5± 16.3	57.1± 21.6
		FaBiAN	61.5± 20.1	57.5± 31.5	53.1± 19.0	80.6± 11.8	72.3± 16.1	59.1± 35.1	52.8± 20.9	54.9± 23.4
		randFaBiAN	68.1± 14.7	62.5± 27.3	59.4± 12.4	83.8± 12.2	80.4± 11.0	70.6± 25.0	62.3± 21.2	57.4± 15.1
		SynthSeg	63.4± 16.8	57.3± 26.8	50.2± 17.6	77.4± 16.0	77.7± 13.4	70.4± 22.0	54.7± 23.9	56.2± 18.2

the FeTA 2024 winning model, *cesne-digair*, highlighting the effectiveness of our approach.

Figure S1 presents a comparison of predicted label volumes between the proposed DRIFTS model and the FeTA 2024 winning model, *cesne-digair*. While some degree of volume discrepancy is expected even under ideal conditions—due to the annotation differences discussed in the paper—this plot enables a direct comparison of how both models estimate tissue volumes, given that they were trained on the same dataset using the same label definitions and should, in principle, exhibit similar biases.

For T2w images, both models show strong agreement with the ground truth volumes across most tissue types. However, in the T1w modality, *cesne-digair* displays substantial deviations from the ground truth for several structures, indicating a failure to generalize to this unseen modality. In contrast, DRIFTS maintains accurate volume estimates even in this challeng-

Table S5: Mean and standard deviation of 95-th percentile Hasudorff distance for the explored models on different testing and training splits. LV - lateral ventricles, CBM - cerebellum, SGM - sub-cortical gray matter, BS - brainstem, mHD95 - average value across all labels.

Testing Splits	Training Split	Experiment	mHD95	CSF	GM	WM	Ventricles	Cerebellum	Deep_GM	Brainstem
CHUV - mial	KISPL-irrk	FetalSynthSeg	2.0± 0.5	1.7± 0.3	1.6± 0.3	2.5± 3.3	2.0± 0.9	1.5± 0.2	2.8± 0.6	2.1± 0.6
		Real data	2.9± 1.2	2.6± 0.8	1.9± 0.5	2.0± 0.3	4.2± 4.4	2.9± 4.7	4.0± 2.8	2.8± 1.1
		FaBiAN	3.6± 1.3	2.6± 0.9	2.2± 0.4	3.6± 0.8	5.3± 4.1	3.5± 6.0	5.0± 2.3	2.9± 1.0
		randFaBiAN	2.1± 0.3	1.8± 0.3	1.6± 0.3	2.1± 0.3	2.1± 0.7	1.6± 0.4	3.0± 0.8	2.6± 1.0
		SynthSeg	2.7± 0.6	2.0± 0.4	2.1± 1.9	2.5± 0.3	3.7± 1.8	2.3± 0.8	3.3± 0.8	2.9± 1.4
	KISPL-mial	FetalSynthSeg	3.1± 0.7	2.7± 1.7	2.5± 0.5	2.2± 0.4	2.6± 1.7	2.9± 2.9	2.6± 0.5	6.3± 0.9
		Real data	3.0± 0.7	2.2± 1.6	2.3± 0.4	2.2± 0.5	3.1± 3.0	1.9± 0.8	2.9± 0.6	6.6± 1.1
		FaBiAN	4.1± 1.4	3.1± 1.9	2.8± 0.6	4.0± 1.2	4.6± 3.4	2.8± 1.7	5.7± 5.2	5.4± 1.3
		randFaBiAN	2.7± 0.6	1.9± 0.6	2.2± 0.5	2.4± 0.5	2.1± 0.6	2.5± 2.2	2.8± 0.7	5.0± 1.2
		SynthSeg	3.4± 0.6	3.5± 2.9	2.4± 0.4	2.9± 0.3	4.6± 1.9	3.1± 1.2	3.2± 0.6	3.9± 0.9
KISPI - irrk	CHUV-mial	FetalSynthSeg	2.5± 1.6	2.4± 2.2	1.6± 0.8	2.2± 1.4	1.9± 1.0	1.5± 0.9	4.3± 4.0	3.4± 3.6
		Real data	9.8± 5.1	9.0± 2.3	7.6± 4.3	5.7± 4.2	6.3± 6.0	16.1± 16.1	9.5± 9.6	14.1± 9.7
		FaBiAN	14.8± 5.3	9.2± 2.1	10.3± 2.2	9.6± 2.7	14.2± 4.3	28.7± 16.6	15.1± 8.7	16.3± 11.1
		randFaBiAN	14.8± 5.1	9.0± 2.0	10.7± 2.3	10.0± 3.2	13.2± 5.5	24.4± 16.5	17.1± 10.1	18.9± 11.3
		SynthSeg	1.5± 0.5	1.3± 1.0	1.2± 0.3	1.4± 0.4	1.4± 0.6	1.3± 0.8	2.0± 0.8	1.7± 0.7
	KISPL-mial	FetalSynthSeg	3.4± 1.7	2.4± 1.5	1.7± 0.8	2.1± 0.7	3.1± 3.4	3.4± 6.5	5.5± 2.9	5.9± 1.4
		Real data	5.9± 4.0	6.3± 4.0	4.1± 4.8	5.4± 6.8	4.3± 4.8	6.3± 10.8	6.8± 4.2	7.8± 4.7
		FaBiAN	14.0± 5.0	9.0± 2.1	10.1± 2.7	11.1± 3.4	8.9± 6.3	24.9± 18.4	18.6± 11.0	15.4± 9.1
		randFaBiAN	5.5± 2.6	6.8± 2.6	3.9± 1.9	3.8± 2.3	5.3± 5.6	6.7± 10.0	6.3± 5.6	5.8± 3.2
		SynthSeg	3.5± 1.4	2.9± 2.0	1.7± 0.8	2.3± 0.7	3.8± 3.2	3.7± 6.3	5.3± 2.0	4.4± 1.3
KISPI - mial	CHUV-mial	FetalSynthSeg	4.1± 2.4	4.8± 4.5	3.2± 1.9	3.4± 1.8	2.4± 2.3	4.5± 3.9	3.8± 3.3	6.4± 3.3
		Real data	5.1± 3.4	5.0± 4.9	3.1± 1.7	2.8± 1.3	4.1± 4.1	7.7± 9.8	4.1± 3.0	8.6± 6.3
		FaBiAN	8.2± 4.3	7.3± 4.9	6.5± 2.4	4.1± 1.4	8.9± 4.4	11.2± 12.4	7.3± 7.7	12.3± 8.7
		randFaBiAN	7.6± 4.2	7.0± 4.8	6.0± 1.8	3.9± 1.4	8.0± 4.4	9.9± 10.6	7.8± 8.1	10.5± 8.1
		SynthSeg	2.6± 1.6	3.1± 3.2	2.2± 2.2	2.6± 3.0	1.7± 1.0	2.5± 1.7	2.7± 3.4	3.6± 4.3
	KISPL-irrk	FetalSynthSeg	3.9± 2.0	3.9± 3.6	2.4± 1.5	2.6± 1.3	2.3± 2.0	3.6± 3.1	5.6± 2.6	6.7± 2.7
		Real data	4.7± 2.7	5.2± 4.6	2.8± 1.7	2.7± 1.4	4.7± 3.9	5.9± 6.5	5.8± 2.6	5.9± 1.8
		FaBiAN	6.5± 3.9	6.5± 4.9	4.7± 3.3	4.4± 2.4	6.4± 5.4	8.3± 7.9	7.0± 5.5	8.4± 6.0
		randFaBiAN	4.1± 2.0	4.4± 4.3	2.8± 1.3	3.1± 2.8	2.2± 1.7	3.5± 2.3	5.7± 2.8	7.0± 2.6
		SynthSeg	5.2± 2.8	4.9± 4.2	3.6± 2.0	3.7± 3.0	4.4± 6.5	5.1± 8.1	6.7± 3.9	7.9± 2.9

Table S6: 95th-percentile Hausdorff Distance (HD95) (mean±std) on FeTA test sets (CHUV, KCL) and dHCP (T1w, T2w). The best (lowest) HD95 for each dataset-contrast pair is shown in **bold**, and the second best is underlined.

Dataset	MR contrast	cesne-digair	FetalSynthSeg	FetalSynthSeg-FT	DRIFTS
CHUV	T2w	2.234±0.399	<u>1.894±0.217</u>	2.064±0.415	1.756±0.225
KCL	T2w	1.694±0.265	1.759±0.254	1.602±0.194	<u>1.642±0.210</u>
dHCP	T1w	10.316±2.056	<u>4.257±0.499</u>	4.154±0.596	4.590±0.705
dHCP	T2w	<u>4.061±0.575</u>	4.091±0.473	4.191±0.502	4.347±0.580

ing setting. Notably, tissues with relatively strong contrast in T1w images, such as CSF, GM, and WM, are estimated more accurately, whereas struc-

Table S7: Per-class segmentation performance (mean \pm std) for Dice and HD95 across experiments and modalities.

Label	MR contrast	FetalSynthSeg		FetalSynthSeg-FT		DRIFTS		cesne-digair	
		Dice	HD95	Dice	HD95	Dice	HD95	Dice	HD95
BSM	T1w	0.784 \pm 0.026	5.536 \pm 0.622	0.784 \pm 0.022	3.204 \pm 0.994	0.776 \pm 0.020	5.232 \pm 0.697	0.046 \pm 0.075	16.558 \pm 5.872
	T2w	0.811 \pm 0.024	5.201 \pm 0.618	0.825 \pm 0.023	4.750 \pm 0.717	0.814 \pm 0.022	5.183 \pm 0.672	0.819 \pm 0.025	4.178 \pm 0.647
CBM	T1w	0.893 \pm 0.022	2.676 \pm 0.722	0.816 \pm 0.034	3.782 \pm 0.680	0.874 \pm 0.023	3.049 \pm 0.668	0.329 \pm 0.182	10.492 \pm 5.700
	T2w	0.913 \pm 0.023	2.609 \pm 0.772	0.897 \pm 0.021	2.773 \pm 0.763	0.907 \pm 0.022	2.749 \pm 0.771	0.880 \pm 0.024	3.082 \pm 0.758
CSF	T1w	0.791 \pm 0.059	1.987 \pm 0.437	0.586 \pm 0.049	3.037 \pm 0.352	0.774 \pm 0.065	2.242 \pm 0.395	0.274 \pm 0.040	5.376 \pm 1.725
	T2w	0.877 \pm 0.049	1.659 \pm 0.510	0.856 \pm 0.026	1.582 \pm 0.314	0.873 \pm 0.037	1.630 \pm 0.377	0.854 \pm 0.028	1.888 \pm 0.341
GM	T1w	0.753 \pm 0.045	1.587 \pm 0.608	0.423 \pm 0.045	2.783 \pm 0.926	0.683 \pm 0.060	2.190 \pm 0.992	0.152 \pm 0.044	5.192 \pm 1.627
	T2w	0.825 \pm 0.044	1.348 \pm 0.539	0.803 \pm 0.037	1.503 \pm 0.579	0.817 \pm 0.044	1.483 \pm 0.661	0.794 \pm 0.051	1.577 \pm 0.706
LV	T1w	0.692 \pm 0.070	10.265 \pm 1.992	0.520 \pm 0.076	7.356 \pm 2.441	0.661 \pm 0.070	11.098 \pm 2.728	0.067 \pm 0.031	12.757 \pm 3.353
	T2w	0.729 \pm 0.070	10.358 \pm 1.972	0.744 \pm 0.054	11.319 \pm 2.484	0.743 \pm 0.062	11.790 \pm 2.438	0.714 \pm 0.052	10.318 \pm 2.921
SGM	T1w	0.799 \pm 0.037	5.808 \pm 0.514	0.764 \pm 0.029	5.839 \pm 0.665	0.791 \pm 0.028	5.829 \pm 0.577	0.108 \pm 0.109	17.901 \pm 5.713
	T2w	0.806 \pm 0.038	5.760 \pm 0.575	0.811 \pm 0.035	5.525 \pm 0.551	0.812 \pm 0.034	5.753 \pm 0.579	0.803 \pm 0.040	5.480 \pm 0.633
WM	T1w	0.893 \pm 0.031	1.940 \pm 0.515	0.776 \pm 0.029	3.080 \pm 0.739	0.859 \pm 0.035	2.488 \pm 0.817	0.649 \pm 0.060	5.654 \pm 2.164
	T2w	0.917 \pm 0.028	1.698 \pm 0.388	0.913 \pm 0.027	1.884 \pm 0.383	0.915 \pm 0.028	1.845 \pm 0.481	0.905 \pm 0.033	1.901 \pm 0.528

tures like the lateral ventricles (LV) and subcortical gray matter (SGM) are poorly predicted by *cesne-digair*.

Interestingly, significant errors were also observed in tissues like the cerebellum (CBM) and brainstem (BSM), which are less dependent on intensity contrast and more reliant on spatial priors. This suggests that the modality-induced domain shift affected not only intensity-related representations but also disrupted the spatial localization capabilities of the model, further highlighting the broad and compounding impact of domain shifts on deep learning model performance.

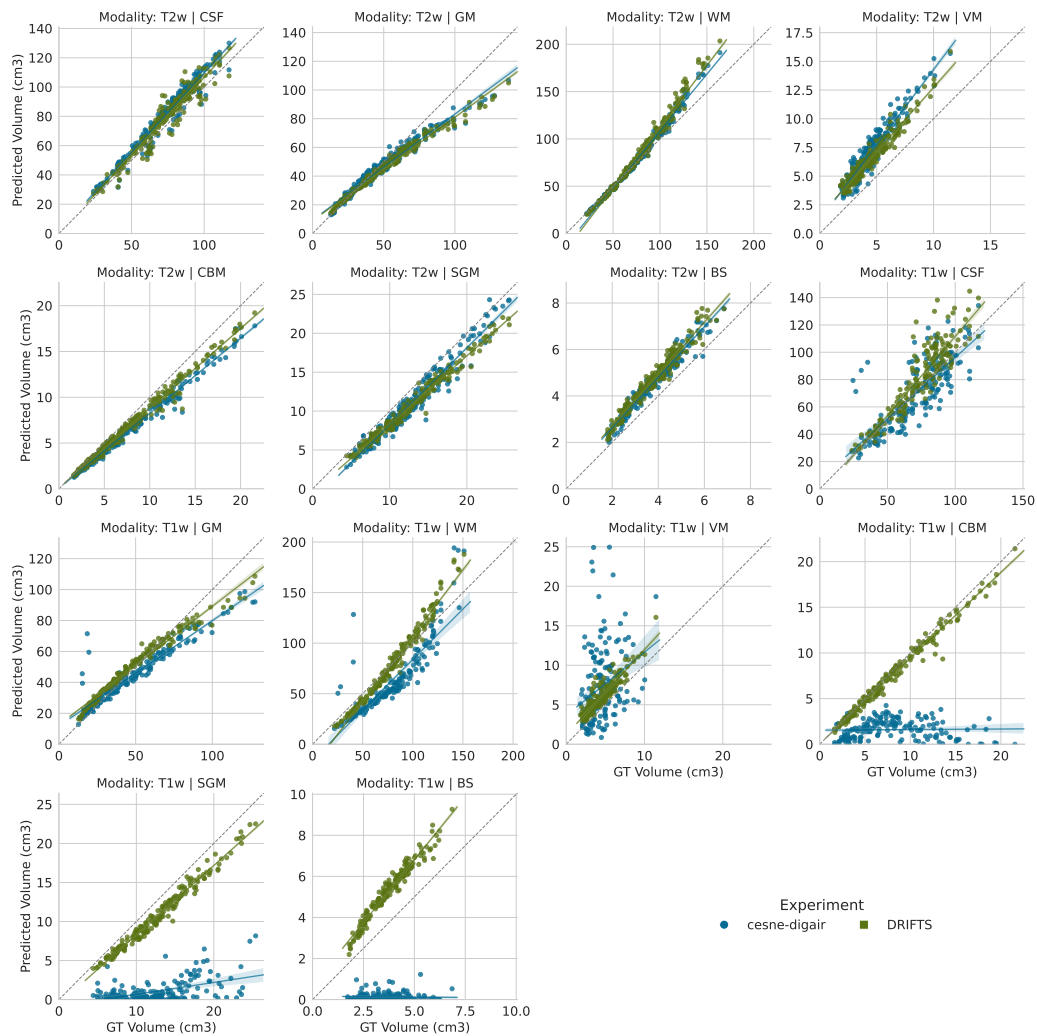


Figure S1: Comparison of predicted and ground truth tissue volumes for dHCP subjects using T1w and T2w images, evaluated with the DRIFTS and *cesne-digair* models. The dotted diagonal line indicates the ideal 1:1 correspondence between predicted and true volumes.